Classification: Chemistry (major); Biophysics and Computational Biology (minor)

Title: **Five-coordinate Mn^{IV} intermediate in the activation of nature's water splitting cofactor.**

Running Title: Five-coordinate Mn^{IV} intermediate of nature's water splitting cofactor.

Authors:

Maria Chrysina, [‡]Eiri Heyno, [,&]Yury Kutin, *Michael Reus, [†]Håkan Nilsson, [‡]Marc M. Nowaczyk, *Serena DeBeer, [§]Frank Neese, [†,a]Johannes Messinger, *Wolfgang Lubitz and [¶]Nicholas Cox

Author affiliations:

*Max-Planck-Institut für Chemische Energiekonversion, Stiftstr. 34-36, D-45470 Mülheim an der Ruhr, Germany; [‡]Plant Biochemistry, Faculty of Biology and Biotechnology, Ruhr-Universität Bochum, Universitätsstr. 150, D-44780 Bochum, Germany; [†]Department of Chemistry, Chemical Biological Centre (KBC), Umeå University, S-90187 Umeå, Sweden; [a]Department of Chemistry – Ångström Laboratorium, Uppsala University, 75120 Uppsala, Sweden; [§]Max-Planck-Institut für Kohlenforschung, Kaiser-Wilhelm-Platz 1, D-45470 Mülheim an der Ruhr, Germany; [¶]Research School of Chemistry, Australian National University, Canberra, ACT 2601, Australia;

[&]Current address: Department of Chemistry and Chemical Biology, TU Dortmund University, Otto-Hahn-Straße 6, 44227 Dortmund, Germany

[¶]To whom correspondence should be addressed: nick.cox@anu.edu.au

Corresponding author:
Nicholas Cox
Phone: +61 2 61258128
E-mail: nick.cox@anu.edu.au

Manuscript information:
Pages: 6
Figs: 4
Tables: 0

Keywords: Photosystem II, WOC/OEC, EPR, EDNMR, methanol

Abbreviations:
PSII – Photosystem II;
OEC – oxygen evolving complex;
EDNMR – electron-electron double resonance-detected NMR.

SI Materials and Methods.

PSII core complex preparations from *Thermosynechococcus (T.) elongatus* were isolated as described previously (1-3). Two preparations were used: a wild type (WT*) and a His-tag strain. Control EPR data measured on PSII core complexes isolated from either strains were identical. Only the His-tag strain could be used for samples in which Ca^{2+} was biosynthetically exchanged with Sr^{2+} (1). This is because PSII containing Sr^{2+} is only stable in the presence of betaine. Owing to the charge of betaine, it cannot be used during the WT preparation protocol. The final buffer of Ca preparations contains: 500 mM mannitol, 40 mM MES (pH = 6.5), 10mM $CaCl_2$, 10mM $MgCl_2$, 0.03% v/v n-dodecyl β-D-maltoside and for Sr: 1.2 M betaine, 40 mM MES (pH = 6.5), 10mM $CaCl_2$, 10mM $MgCl_2$, 0.03% v/v n-dodecyl β-D-maltoside, 10% v/v glycerol. The chlorophyll concentration for W-band samples is ≈ 5 mg/mL and ≈ 2.5 mg/mL for Q band samples. Phenyl-p-benzoquinone (PpBQ) dissolved in dimethyl sulfoxide (DMSO) was added as electron acceptor at a final concentration of 0.5 mM. Samples were poised at S_1 by a pre-flash using an Nd-YAG laser (wavelength 532 nm) and dark-incubated at room temperature for one hour. The S_3-state was generated by two flashes using an Nd-YAG laser and the sample was immediately frozen in liquid N_2. For samples with added methanol PpBQ was instead dissolved in methanol. The final concentration of methanol was 3% or 5% v/v. For ammonia samples: 1 M NH_4Cl in 1 M HEPES (pH = 7.6) was added at a ratio of 1:10 v/v to the sample, i.e. giving a final concentration of 100 mM, which equates to 2 mM NH_3 in solution.

W-band pulse EPR measurements were performed using a Bruker ELEXSYS E680 spectrometer at T = 4.8 K. Electron spin echo (ESE)-detected field-swept spectra were measured using the pulse sequence: t_p–τ–2t_p–τ–*echo*. The length of the π/2 microwave pulse was generally set to t_p = 8 ns for the S_3-state EPR spectra and t_p = 20ns for the Y_D radical. The interpulse distance was set to τ = 240 ns. Electron spin nutation curves were measured using the pulse sequence: t_{prep}–T–t_p–τ–2t_p–τ–*echo*. The preparation pulse length (t_{prep}) was incremented over the range of 4-1000 ns in 4 ns steps. The length of the π/2 microwave pulse was t_p = 16 ns and the interpulse delays were T = 3.0 μs and τ = 500 ns. ELDOR-detected NMR (EDNMR) spectra were collected using the pulse sequence: t_{HTA}–T–t_p–τ – t_p–τ–*echo* (4). The high turning angle (HTA) microwave pulse was applied at microwave frequency ν_{mw}. The detection pulse sequence t_p–τ–2t_p–τ–*echo*, applied at the microwave frequency matched to the cavity resonance, was set at T = 1 μs after the HTA pulse to ensure near-complete decay of the electron spin coherencies. The π/2 pulse length used for detection was t_p = 80 ns, and the inter-pulse separation was τ = 250 ns. The back-half of the echo was integrated over 300 ns starting from its maximum. The spectra were acquired by continuously sweeping the HTA frequency ν_{mw} at a fixed B_0 in steps of 1.88 MHz. The length and amplitude of the HTA microwave pulse was set to 5 μs and at ω_1 = 4.7 x 10^7 $rads^{-1}$ ($\Delta\nu_{1/2}$ ≈ 15 MHz) respectively.

Q-band pulse EPR measurements were performed at 7 K using a Bruker ELEXSYS E580 Q-band pulse spectrometer equipped with a home-built TE011 microwave resonator (5) and a cryogen-free variable temperature cryostat from Cryogenic Ltd. ESE-detected field-swept spectra were measured using the same settings as W-band: a π/2 microwave pulse length of t_p = 8 ns for the S_3-state EPR spectra and t_p = 20 ns for the Y_D radical and an interpulse distance of τ = 240 ns. For ^{55}Mn-ENDOR experiments the Davies pulse sequence was used: t_{inv}–t_{RF}–T–t_p–τ–2t_p–τ–*echo*, where t_p = 10 ns and τ = 240 ns. The inversion microwave pulse was t_{inv} = 20 ns, and the radio frequency (RF) π pulse was t_{RF} = 3.5 μs. The RF frequency was swept between 10 and 260 MHz in 1.05 MHz steps.

Time resolved membrane inlet mass spectrometry experiments were performed in a stirred, temperature controlled (20°C) membrane-inlet cell (165 μl volume), connected to a magnetic sector field isotope ratio mass spectrometer (ThermoFinnigan Delta^{Plus} XP) via a cooling trap (liquid N_2). Samples were loaded in darkness. After 20 minutes of degassing, the sample was advanced to the S_3 state with two saturating Xe-lamp flashes. Subsequently the sample was rapidly enriched with $H_2{}^{18}O$ (97%, 8 ms mixing time) and one additional flash was applied, generating O_2. The delay between the enrichment and the last flash was incremented between 8 ms to 10 s. The final ^{18}O sample enrichment was 22%. Molecular oxygen dissolved in the $H_2{}^{18}O$ was removed from the delivery syringe (modified Hamilton CR-700-50) by glucose/glucose oxidase and catalase (6). After 5 minutes 4 additional flashes were given at 2 Hz and used for normalization. Data analysis was performed as described earlier (6-8)

SI EPR Theory

Electron-spin nutation measurements. As described in (9), the magnitude of the pulse EPR signal is dependent of the length of the nanosecond microwave pulses. The optimal length (π flip angle β_0) of such pulses is a property of the spin state of the species being measured. For a given EPR transition, i.e. $\phi_a \rightarrow \phi_b$, the flip angle is defined as the square root of the transition probability connecting the two levels (10):

$$\beta_0 = \sqrt{P_{ab}} = \sqrt{\left|\phi_a\middle|\hat{H}_1\middle|\phi_b\right|^2} \quad \textbf{(Eq. S1)}$$

where $\hat{H}_1$ describes the transient magnetic field associated with the applied microwave pulse:

$$\hat{H}_1 = \beta_e \cdot \vec{B}_1 \cdot \hat{g} \cdot \vec{S} - \beta_n \cdot g_n \cdot \vec{B}_1 \cdot \vec{I} \quad \textbf{(Eq. S2)}$$

In a system with multiple unpaired electrons, a set of pre-factors are introduced into the $\hat{H}_1$ matrix associated with the ladder operators S^+ and S^-.

$$S^+ \left| S \quad M_s \right\rangle = \hbar\sqrt{S(S+1) - M_s(M_s+1)}\,\left| S \quad M_s + 1 \right\rangle$$
$$S^- \left| S \quad M_s \right\rangle = \hbar\sqrt{S(S+1) - M_s(M_s-1)}\,\left| S \quad M_s - 1 \right\rangle$$
(Eq. S3)

As a result, the probability of an EPR transition associated with an S = ½ spin manifold, as compared to the transition probabilities (of allowed transitions) of a high-spin system, are always smaller, and hence the optimal π pulse length for a S = ½ system is longer. In this study we used the most prominent feature of the modified S_3 state spectrum to determine the ground spin state, i.e. the low-field edge, which does not overlap with the untreated (S_3^{Ca}) spectrum. As shown in **Figure 3a** of the main text, the intensity of the modified S_3 EPR signal oscillates with a microwave nutation period of 130 ns. The period is 2.25 (approximately √6) times shorter than that seen for the tyrosine $Y_D^{\bullet}$ radical, an internal S = ½ probe which is used to calibrate the measurement. This is consistent with this transition representing the $M_s = \pm|3\rangle \rightarrow \pm|2\rangle$ transition (**Eq. S3**) of an S_G = 3 spin manifold. The small deviation of this value from the predicted one (8%) is likely due to a degree of M_s level mixing, a consequence of the large D value.

Simulation of the EPR spectra using the spin Hamiltonian formalism. EPR spectra were fitted assuming an effective spin S = 3 ground state, as constrained by the electron spin nutation

experiments discussed above. The basis set that describes the Mn-tetramer spin manifold can be built from the product of the eigenstates of the interacting spins (9):

$$|3 \quad M_S \quad I_1 \quad I_2 \quad I_3 \quad I_4 \quad m_1 \quad m_2 \quad m_3 \quad m_4\rangle \qquad \textbf{(Eq. S4)}$$

Here M_S refers to the electronic magnetic sub-level, 3, 2, 1, 0, -1, -2, -3; I_i takes the value 5/2; and the corresponding m_i terms have the values $-I_i$, $1\text{-}I_i$, ..., $I_i\text{-}1$, I_i. The spin Hamiltonian that describes the spin manifold is:

$$\begin{aligned}\hat{H} = D\left[\vec{S}_z^2 - \frac{1}{3}S(S+1) + \frac{E}{D}\left(\vec{S}_x^2 - \vec{S}_y^2\right)\right] \\ + \frac{a}{6}\left[\vec{S}_x^4 + \vec{S}_y^4 + \vec{S}_z^4 - \frac{1}{5}S(S+1)(3S^2+3S-1)\right] \\ + \frac{F}{180}\left[35\vec{S}_z^4 - 30S(S+1)\vec{S}_z^2 + 25\vec{S}_z^2 - 6S(S+1)\right. \\ \left. + 3S^2(S+1)^2\right] + g\beta\vec{B}_0\cdot\vec{S} \\ + \sum_{i=1}^{4}(-g_n\beta_n\vec{B}_0\cdot\vec{I}_i + \vec{S}\cdot A_i\cdot\vec{I}_i) \qquad \textbf{(Eq. S5)}\end{aligned}$$

It contains: i) second- and fourth-order zero field splitting terms describing the energy-ladder of the spin system at zero-field (parameterized in terms of *D*, *E*, *a* and *F*). Note the fitted cubic (*a*) and axial (*F*) forth order parameters are small (<5% *D*, *E*). Their inclusion does not change the overall shape of the spectrum but they are needed to accurately reproduce the turning points of the spectrum; ii) the electron Zeeman term describing the (effective) electron spin interaction with the applied magnetic field; iii) the set of nuclear Zeeman terms, describing the interaction of the nuclear spins with the applied magnetic field; and iv) the set of hyperfine terms describing the interaction between the (effective) electron spin *S* and each nuclear spin I_i. For the simulations of the field-swept EPR spectra, only the first four terms (zero-field splitting and electron Zeeman) were used. For simulations of the double resonance (EDNMR) data, the full Hamiltonian was used assuming ENDOR transition intensities and correcting for the resonator bandwidth - the effect of the resonator bandwidth is to reduce the intensity of the higher frequency lines relative to the lower frequency lines. This approximation is valid because the EPR spectrum is very broad (≈2 T) and the HTA pulse used to pump the transition highly selective (bandwidth ≈1 MHz). As such the EDNMR spectrum collected at a particular field position represents a single crystal-like orientation and thus will not suffer from lineshape artifacts seen for powder EDNMR signals (11, 12).

Analyzing EDNMR spectra of integer spin systems. When measuring a hyperfine spectrum of a spin $S = ½$ species, nuclei which couple to the electron spin will give rise to a doublet either: i) centered about the nuclear Larmor frequency (ν_L), split by the hyperfine coupling (weak coupling case); ii) centered about one half the hyperfine coupling, split by twice the nuclear Larmor frequency (strong coupling case). For an S > 1/2 system, the structure of the hyperfine spectrum depends on which EPR transition ($M_S \leftrightarrow M_S$+1) is used to observe the nuclear transitions. First-order expressions below describe the positions of the two doublet peaks for the $M_S \leftrightarrow M_S$+1 transition:

$A/2 > \nu_L$ (strong coupling case):

$$\begin{aligned}\nu_\alpha &= |(M_s+1)A| - A/|A|(|M_s+1| - |M_s|)\nu_L \\ \nu_\alpha' &= |M_sA| - A/|A|(|M_s+1| - |M_s|)\nu_L\end{aligned} \qquad \textbf{(Eq. S6)}$$

$\nu_L > A/2$ (weak coupling case):

$$\begin{aligned}\nu_\alpha &= |\nu_L| - (M_s+1)A \\ \nu_\alpha' &= |\nu_L| - M_sA\end{aligned} \qquad \textbf{(Eq. S7)}$$

Interpreting EPR parameters measured in exchange-coupled systems. As stated in the main text, the measured EPR parameters for an oligonuclear transition metal complex are a property of both the site properties of the individual metal ion and the network of exchange couplings (J_{ij}) which modulate the contribution of each ion to the effective electronic spin state. The ladder of effective spin states can then be modeled by the Heisenberg Hamiltonian:

$$\hat{H} = -2\sum_{i\neq j} J_{ij}\,\vec{S}_i\cdot\vec{S}_j \quad \textbf{(Eq. S8)}$$

In EPR spectroscopy we can usually only access the ground spin state; the ground state for the S_3 state is $S = 3$ as described above. The spin Hamiltonian parameters determined for this 'fictitious' spin state need to be scaled to allow comparison to single ion values for which model complex data exist. These scaling factors are termed spin projection factors (ρ_i). A projection (contribution) is defined as the ratio of the on-site spin expectation value $\langle S_z^i\rangle$ to the 'total spin' *S* or equally $\langle S_z\rangle$:

$$\rho_i = {\langle S_z^i\rangle}/{S} \qquad \textbf{(Eq. S9)}$$

There are explicit formulae for the two spin projections in the case of a two spin system (S_1, S_2):

$$\rho_1 = \frac{S_1(S_1+1) - S_2(S_2+1) + S(S+1)}{S(2S-1)} \qquad \textbf{(Eqs. S10)}$$

$$\rho_2 = \frac{S_2(S_2+1) - S_1(S_1+1) + S(S+1)}{S(2S-1)}$$

And in the instance where the system contains only ferromagnetic couplings the spin projection of each site scales with the number of unpaired electrons associated with each site. The measured (projected) parameter is then calculated by multiplying the site parameter by the corresponding spin projection coefficient. In the case of the set of projected hyperfine tensors this is:

$$\hat{A}_i = \rho_i\hat{a}_i \qquad \textbf{(Eq. S11)}$$

Whereas the projected fine structure splitting tensor is the sum over all site fine structure value (d_i) multiplied by its respective spin projection factor (κ_i):

$$\hat{D} = \sum_i \kappa_i\hat{d}_i \qquad \textbf{(Eq. S12)}$$

Note that when scaling the site fine structure values a second spin projection factor (κ_i) is used defined as the ratio of the expectation value of the spin operator $\langle S_{i,z}^2 - \frac{1}{3}S_i(S_i+1)\rangle$ of the i^{th} Mn to the expectation value of the spin operator $\langle S_z^2 - \frac{1}{3}S(S+1)\rangle$ or equally $\frac{1}{3}S(2S-1)$:

$$\kappa_i = 3\frac{\langle S_{i,z}^2 - \frac{1}{3}S_i(S_i+1)\rangle}{S(2S-1)} \qquad \textbf{(Eq. S13)}$$

It is noted that as the spin projection coefficients (κ_i) scale with the square of the inverse of the total spin of the effective spin state $\frac{1}{3}S(2S-1)$, the *D* value typically decreases as for higher spin states. This should be taken into account when comparing *D* values of complexes with a different effective ground spin state (see equation **Eq. 1** main text). Note **Eq. 1** is only robust when comparing complexes of similar coupling topology and nuclearity.

SI Text

X-band EPR measurements were performed to check protocols for ammonia addition and Ca^{2+}/Sr^{2+} exchange (**Fig. S1**). Both of these treatments are known to modify the S_2 state EPR spectrum, a structured S = ½ signal 200 mT wide (at X-band), centered at g = 2. The S_2 state was prepared by continuous wave (CW) 200 K illumination. Samples treated with ammonia were subsequently annealed in the dark at -10 °C for 30 s to allow the NH_3 to bind to the cofactor. The S_2 state spectrum of the ammonia bound (S_2^{NH3}) and Mn_4O_5Sr cofactor both displayed characteristic changes in line positions and intensities as compared to wild type (S_2^{Ca}). Changes in the S_2 multiline spectrum have been previously interpreted as representing only a small modification of the electronic structure of the cofactor (13-16). Note, for PSII prepared from *T. elongatus*, the S_2 state spectrum is unchanged by the addition of methanol (17).

Data subtractions for Q- and W-band S_3 state EPR data. All PSII samples display additional EPR signals not associated with the Mn_4O_5Ca cofactor. These signals are unchanged by the short flash illuminations used to progress the cofactor through the S-state cycle. As a consequence, a clean cofactor spectrum in the S_3 state can be isolated by subtracting the dark spectrum (S_1 state, **Figs. S2-S7** left-hand side) from the one recorded after two light flashes. Since the S_1 state does not have a perpendicular mode EPR signal, the dark spectrum represents only the oxidized cytochrome (Fe^{III}) signals from the PsbV subunit and possibly cyt$_{b559}$ subunits of PSII. Both low- and high-spin cytochrome signals are observed. The low-spin (S = ½) cytochrome signal with turning points at g = [3.0, 2.5, 1.9] strongly overlaps with the S_3 state spectrum. There is a smaller high-spin cytochrome signal (S = 5/2) with a main turning point at 1 T, which is outside the S_3 spectrum. A free Mn^{II} (S = 5/2) signal of varying intensity stems from a small fraction of damaged PSII centers (<5%). It has a characteristic six-peak structure, which is observed in the center of all S_3 spectra.

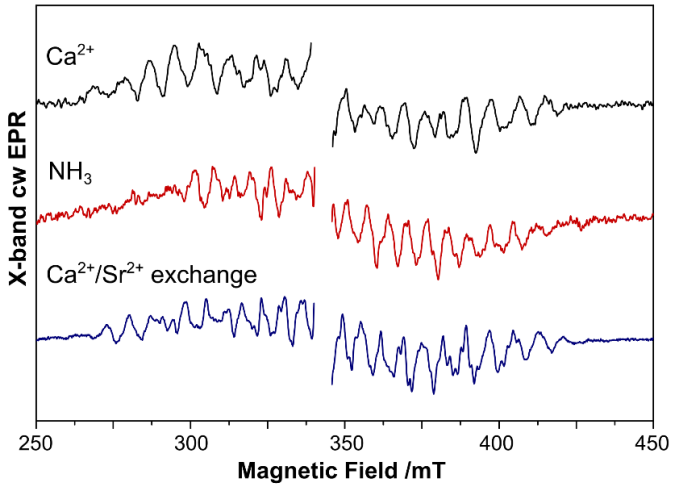

Figure S1. X-band CW-EPR spectra of *T. elongatus* poised in the S_2 state: black – control (Mn_4O_5Ca), red – NH_3-treated and blue – upon Ca^{2+}/Sr^{2+} exchange (Mn_4O_5Sr). The S_1 state background of cytb_{559} and cytc_{550} was subtracted from the data after illumination. In all samples the $Y_D^{\bullet}$ signal centered at g ≈ 2 was removed for clarity of presentation. **Experimental parameters**: microwave frequency: 9.6265 GHz (control), 9.6375 GHz (NH_3), 9.6367 GHz (Sr); microwave power: 6.3 mW; modulation amplitude: 7 G; sweep time: 336 s; time constant: 164 ms; temperature: 10 K (NH_3), 8 K (Sr and control).

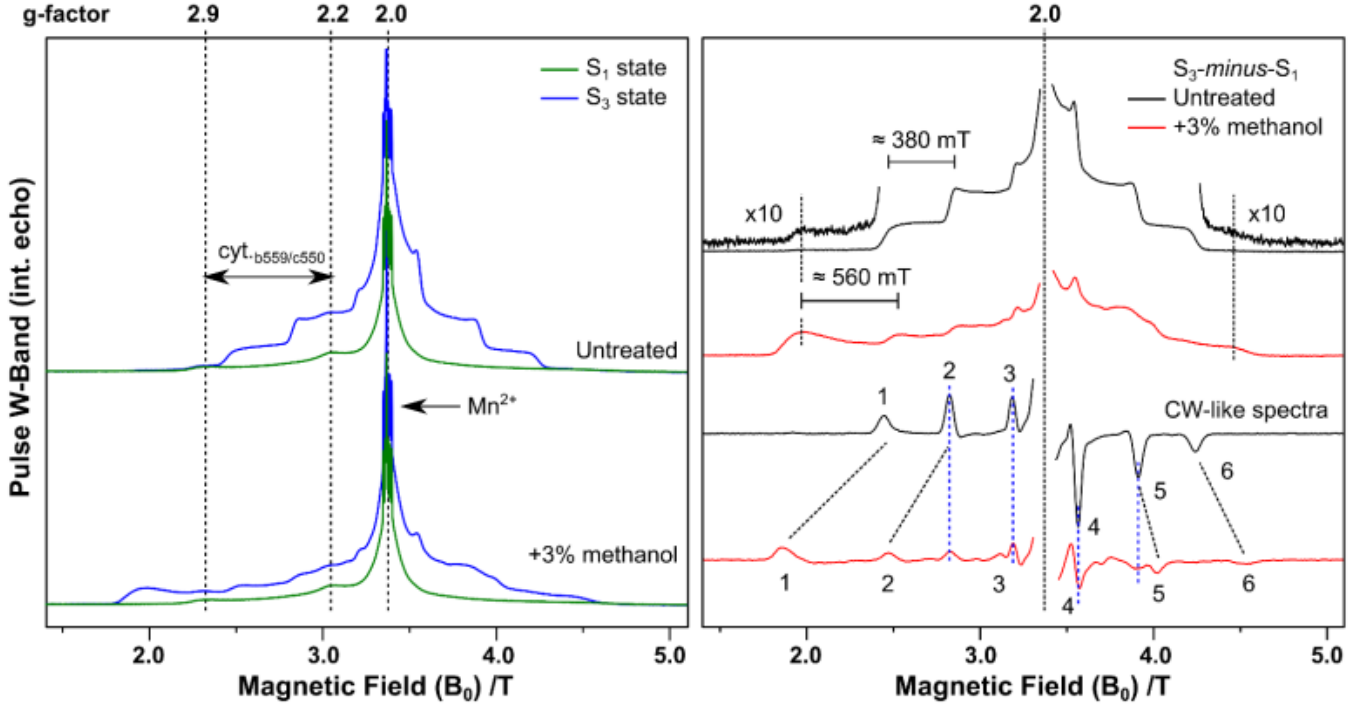

Figure S2. **Left panel:** W-band ESE-detected field-swept S_3 (blue) and S_1 (green) spectra for a 0% (untreated) and 3% v/v methanol-treated sample. Mn^{II}, cytb_{559} and cytc_{550} signals are marked. **Right panel:** S_3-*minus*-S_1 spectra for the untreated (black) and 3% methanol (red) samples with the respective pseudo-modulated representation shown (bottom two traces). A small signal with a spectral width similar to that of methanol-treated PSII is observed in the untreated sample (magnified by the factor of 10). In the pseudo-modulated spectra the peak positions are better resolved. The broadening of the S_3 spectrum due to methanol (black dashed lines), and the contribution of the untreated S_3 in the methanol-treated sample (blue dashed lines) are marked. Tyr_D and Mn^{II} signals were deleted for clarity. **Experimental parameters:** microwave frequency: 94 GHz, shot repetition period: 0.5 ms, field axis: 3800 pts, temperature 4.8 K. Each spectrum represents 1024 averages (1024 shots per point, 1 scan).

Description of S_3 state W-band EPR spectra. W-band EPR spectra of the Mn cofactor poised in the S_3 state are shown in **Figs. 3, S2-3, S5-7**. The absorption spectrum for the S_3^{Ca} and S_3^{NH3} is centered at 3.4 T ($g \approx 2$) and consists of four superimposed tiers or, equally, six evenly spaced lines (see pseudo-modulated transform, excluding $g \approx 2$ region) separated by 0.4 T. The absorption spectrum for S_3^{MeOH} and S_3^{Sr} also contains approximately four superimposed tiers or, equally, six lines (see pseudo-modulated transform) now separated by 0.6 T. These spectra are also more asymmetric about 3.4 T ($g \approx 2$), with the high field edge closer to $g = 2$ than the low field edge.

The large spectral breadth of these signals (1.5 to 2.5 T) indicates that they arise from an effective spin state with several effective unpaired electron spins. As described earlier, spin nutation measurements constrain the number of unpaired electrons associated with the ground state of the spin manifold to be six. These six unpaired electrons give rise to seven non-degenerate energy (M_S) levels in a magnetic field and thus six allowed EPR transitions (**Fig. S9**).

In the absence of a zero-field splitting interaction all EPR transitions would be observed at $g = 2$. Inclusion of the zero-field splitting leads to a spreading of the EPR transitions, with those between the highest and lowest M_S values, i.e. $|-3\rangle \rightarrow |-2\rangle$ and $|+2\rangle \rightarrow |+3\rangle$ shifting furthest from $g = 2$. The effect of the zero-field splitting term is dependent on the orientation of the cofactor relative to the magnetic field (see **Fig. S9**). As our measurements are performed on frozen solution (powder) samples measured at cryogenic temperatures, all orientations of the cofactor relative to the magnetic field are sampled evenly and thus all contribute to the total spectrum.

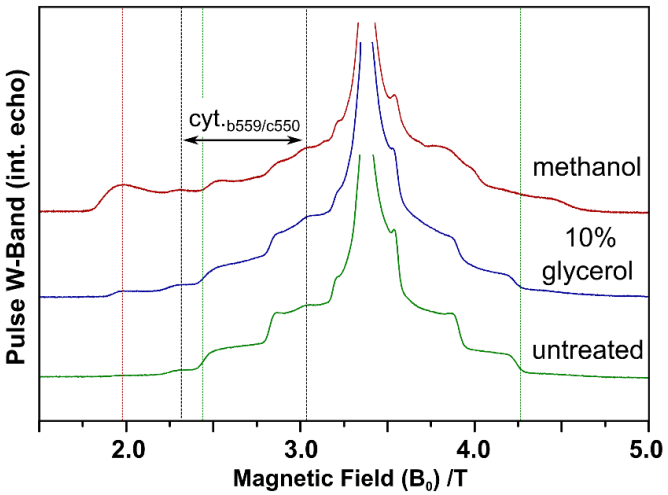

Figure S3: W-band ESE-detected field-swept spectra of the untreated S_3 (green), S_3 with 10% glycerol (blue), 3% methanol (red). Cytochrome signals are marked with grey lines. The untreated S_3 signal is marked by green lines and the new signal by a red dotted line. In the untreated system, almost 100% of centers are represented by the S_3^{Ca} signal. However the addition of only 10% glycerol introduced an appreciable S_3^{MeOH}-like signal, making up 20% of centers.

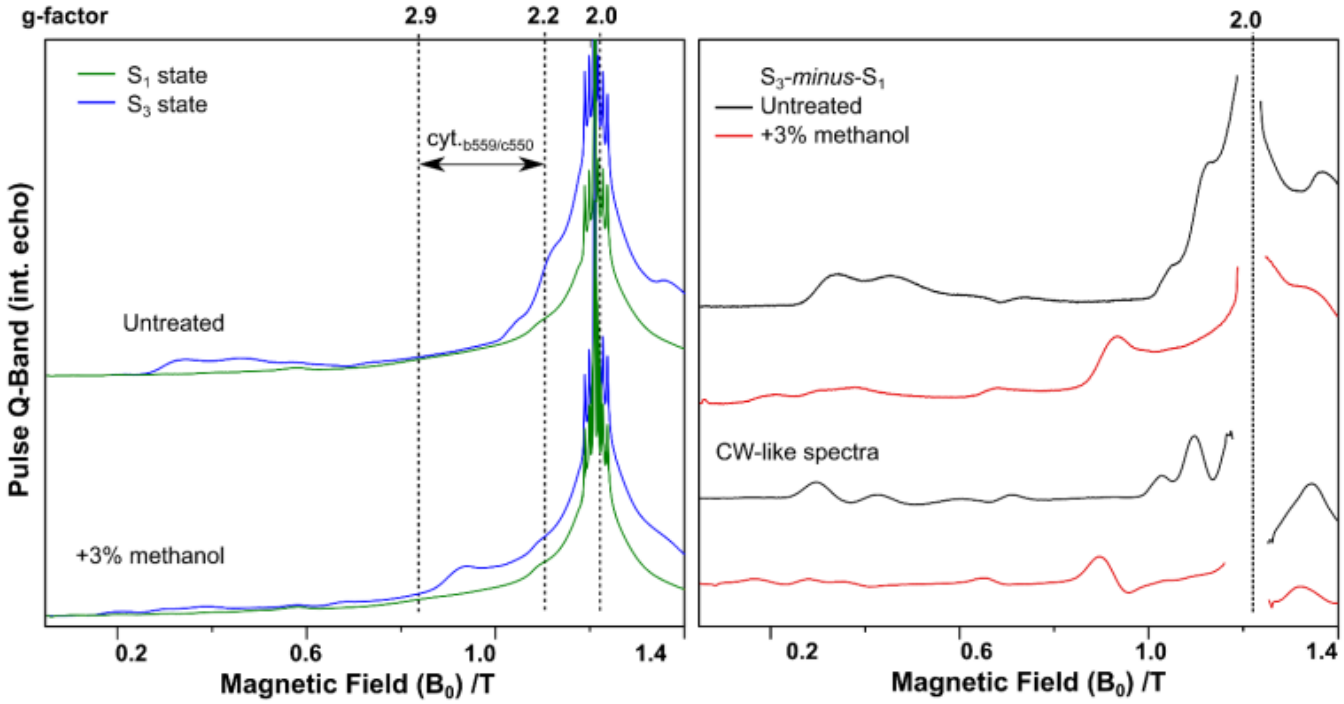

Figure S4. **Left panel:** Q-band ESE-detected field-swept S_3 (blue) and S_1 background (green) spectra for a 0% (untreated) and 3% v/v methanol-treated sample. **Right panel:** S_3-*minus*-S_1 spectra for the untreated (black) and 3% methanol (red) samples with the respective pseudo-modulated representation shown (bottom two traces). Tyr_D and Mn^{II} signals were deleted for clarity. **Experimental parameters:** microwave frequency: 34 GHz, shot repetition period: 0.5 ms, field axis: 4096 pts, temperature: 7 K. Each spectrum represents 2048 averages (1024 shots per point, 2 scans).

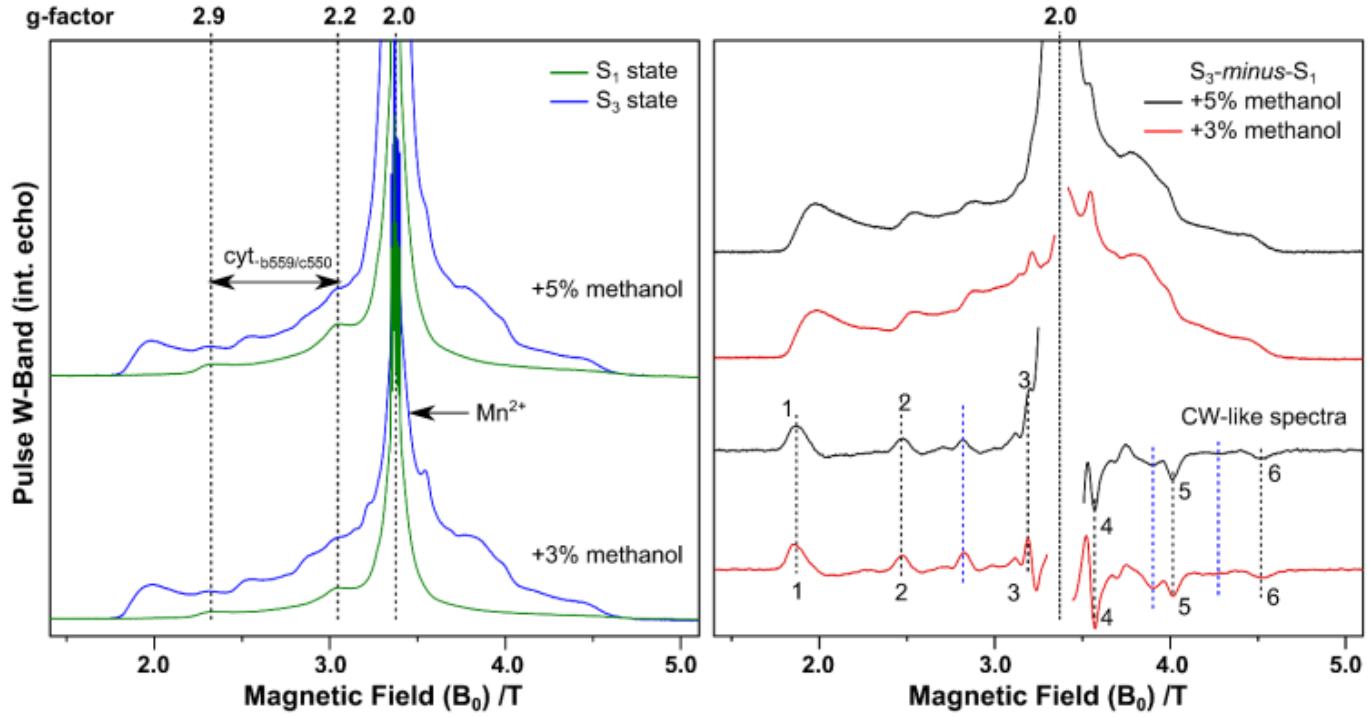

Figure S5. Left panel: W-band ESE-detected field-swept S_3 (blue) and S_1 background (green) spectra for a 3% and 5% v/v methanol-treated sample. Mn^{II}, cytb_{559} and cytc_{550} signals are marked. **Right panel:** S_3-*minus*-S_1 spectra for the 5% (black) and 3% (red) methanol samples with the respective pseudo-modulated representation shown (two bottom traces). The different contributions of the untreated S_3 in the two methanol-treated samples are marked with blue dashed lines. Tyr_D and Mn^{II} signals were deleted for clarity. **Experimental parameters:** microwave frequency: 94 GHz, shot repetition period: 0.5 ms, field axis: 3800 pts, temperature: 4.8 K. Each spectrum represents 1024 averages (1024 shots per point, 1 scan).

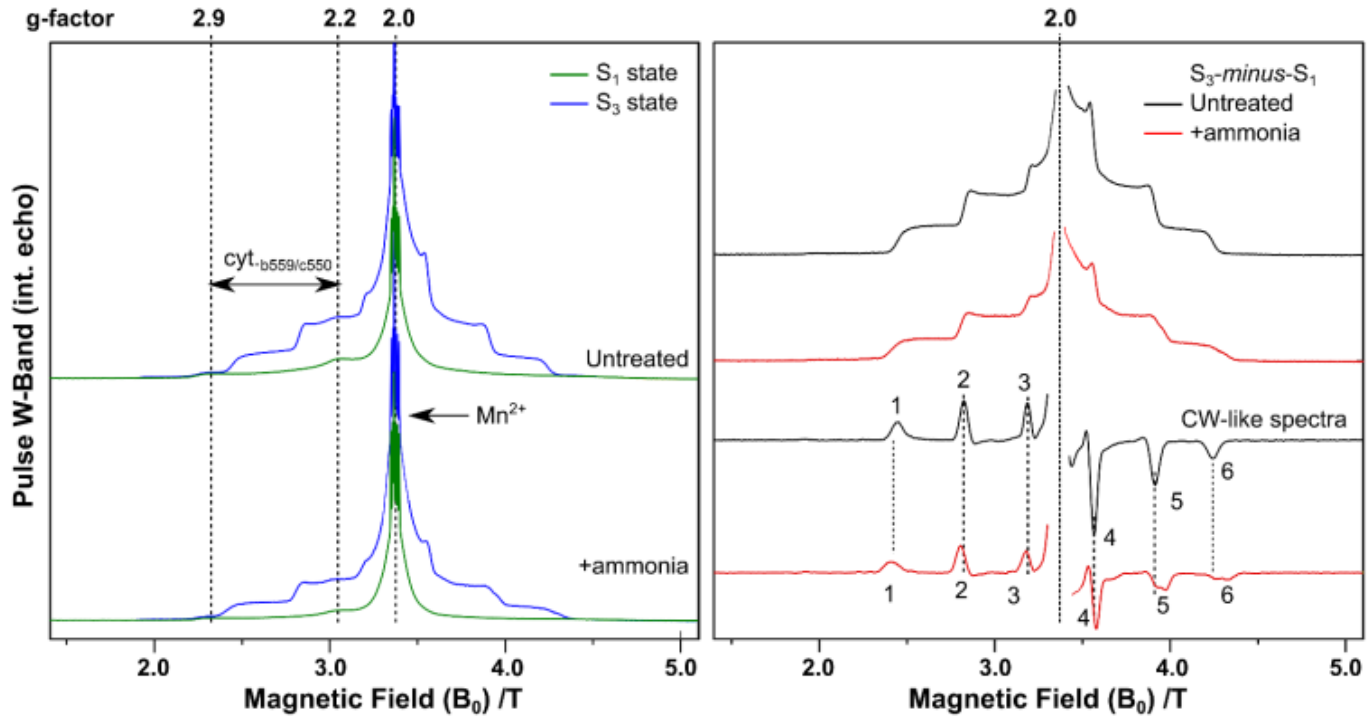

Figure S6. Left panel: W-band ESE-detected field-swept S_3 (blue) and S_1 background (green) spectra for an untreated and ammonia-treated sample. Mn^{II}, cytb_{559} and cytc_{550} signals are marked. **Right panel:** S_3-*minus*-S_1 spectra for the untreated (black) and ammonia-treated (red) samples with the respective pseudo-modulated representation shown (two bottom traces). Tyr_D and Mn^{II} signals were deleted for clarity. **Experimental parameters:** microwave frequency: 94 GHz, shot repetition period: 0.5 ms, field axis: 3800 pts, temperature: 4.8 K. Each spectrum represents 1024 averages (1024 shots per point, 1 scan).

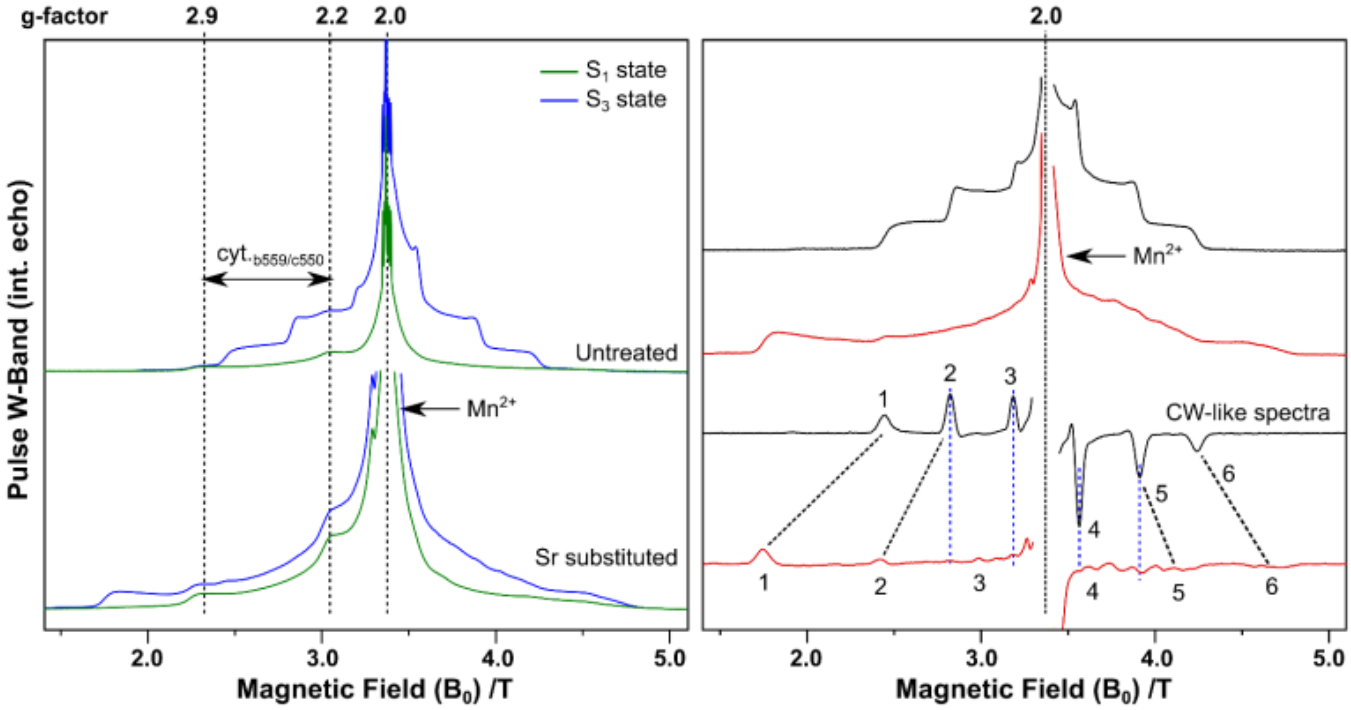

Figure S7. Left panel: W-band ESE-detected field-swept S_3 (blue) and S_1 background (green) spectra for an untreated and Sr^{2+}-substituted sample. Mn^{II}, cytb_{559} and cytc_{550} signals are marked. **Right panel:** S_3-*minus*-S_1 spectra for the untreated (black) and Sr-substituted (red) samples with the respective pseudo-modulated representation shown (two bottom traces). Broadening of the S_3 spectrum due to the Sr-substitution is marked by black dashed lines. Tyr_D and Mn^{II} signals were deleted for clarity. **Experimental parameters:** microwave frequency: 94 GHz, shot repetition period: 0.5 ms, field axis: 3800 pts, temperature: 4.8 K. Each spectrum represents 1024 averages (1024 shots per point, 1 scan).

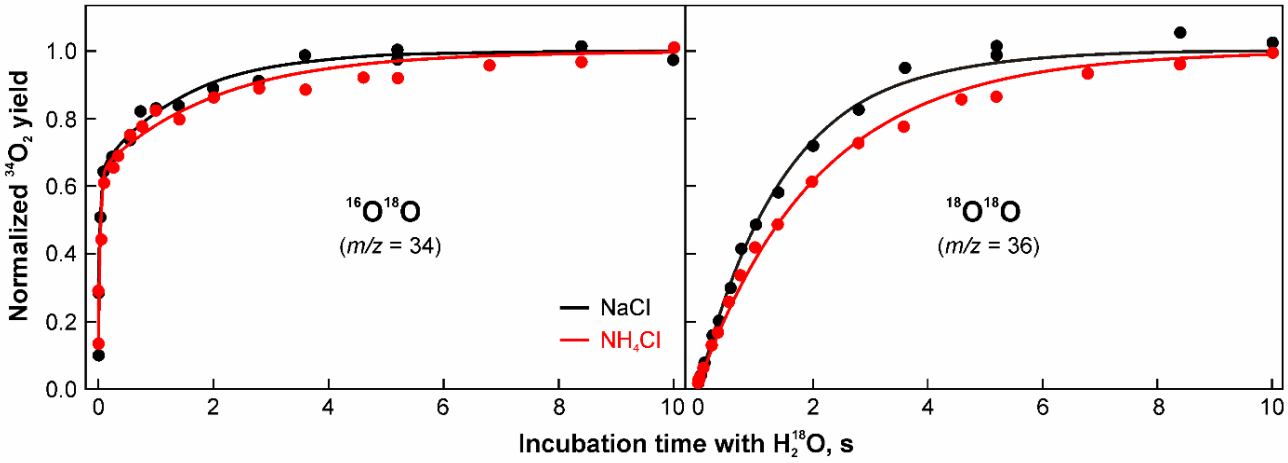

Figure S8. Time-resolved membrane inlet mass spectrometry traces monitoring substrate exchange in the S_3 state at pH 7.6 in the presence of either 100 mM NH_4Cl (red dots) or 100 mM NaCl (black dots). The lines represent biexponential ($^{34}O_2$, Left) and monoexponential ($^{36}O_2$, Right) fits. NH_4Cl: k_f = 28 s^{-1}, k_s = 0.5 s^{-1}. NaCl: k_f = 29 s^{-1}, k_s = 0.6 s^{-1}.

Table S1: Fitted spin Hamiltonian second-order (*D*, *E/D*) and fourth-order (*a*, *F*) zero-field parameters for the EPR lineshape simulations in **Fig. 3** and **Fig. S11**

	Species *% of centers*	*D* /cm^{-1}	*E/D*	*a* /MHz	*F* /MHz
S_3^{Ca}	100%	-0.173	0.30	-155	150
S_3^{NH3}	1 (43%)	-0.175	0.30	-175	150
	2 (57%)	-0.182	0.33	-205	200
S_3^{MeOH}	1 (20%)	-0.173	0.30	-155	150
	2 (80%)	-0.281	0.16	20	-40
S_3^{Sr}	1(17%)	-0.173	0.30	-155	150
	2 (28%)	-0.303	0.15	-95	0
	3 (56%)	-0.303	0.22	-170	150

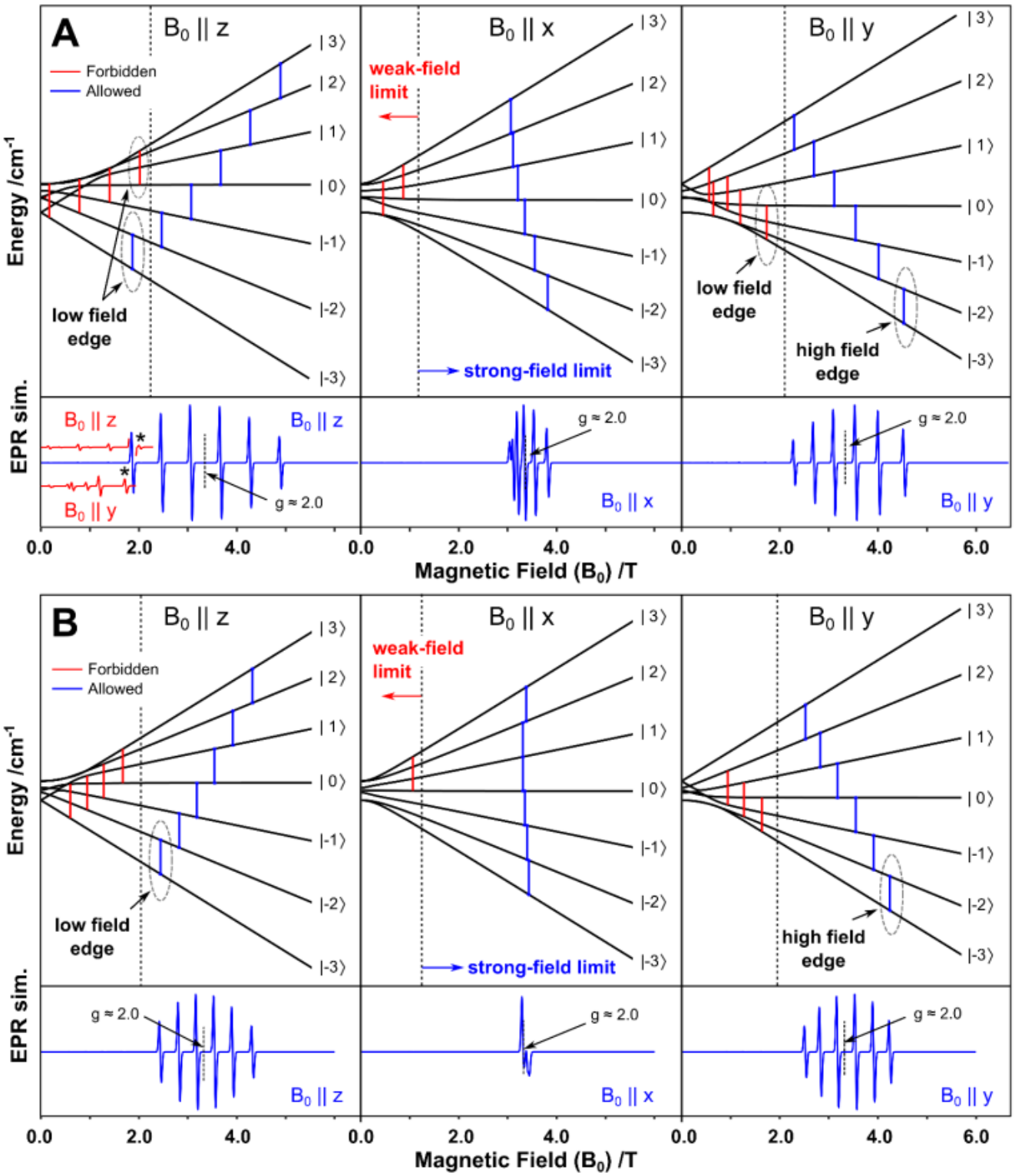

Figure S9. A) Energy level diagrams for the S_3^{MeOH} (S_3') EPR signal. The three panels correspond to the B_0 field aligned along the three principal axes of the D-tensor: D_Z, D_X and D_Y. The blue and red vertical lines represent allowed and forbidden EPR transitions. Predicted single crystal EPR spectra are shown underneath. **B)** Corresponding energy level diagrams for the S_3^{Ca} EPR signal.

Electronic structure of the S_3 and S_3' cofactor. The observed high-spin ground state of $S = 3$ for the S_3 state requires that the Mn ions are coupled by dominantly ferromagnetic (F) exchange interactions – although there must be at least one antiferromagnetic (AF) interaction. As we describe below, it is the number of AF couplings that determines the electronic coupling topology of the cofactor, which can be experimentally accessed by measuring the hyperfine couplings associated with the four ^{55}Mn nuclei.

There are only two coupling topologies possible for the cofactor in the S_3 state (**Fig. S10**). The overall structure of the complex embedded in the protein requires the Mn ions of the cubane unit (Mn1 and Mn2, Mn2 and Mn3) to couple together ferromagnetically, and the external Mn ion (Mn4) to couple to Mn3 antiferromagnetically (αααβ). However one coupling pathway can potentially change depending on the precise structure of the cofactor, the exchange pathway between Mn1 and Mn3. In structures which contain a closed cubane (S_2^B-like) this pathway is F, whereas in structures which contain an open cubane (S_2^A-like) this pathway is AF. Note the final S_3 state (S_3^{Ca}) with an addition of a water-derived ligand bound at Mn1 can be considered as containing an open cubane. This subtle change has a dramatic consequence for the coupling topology:

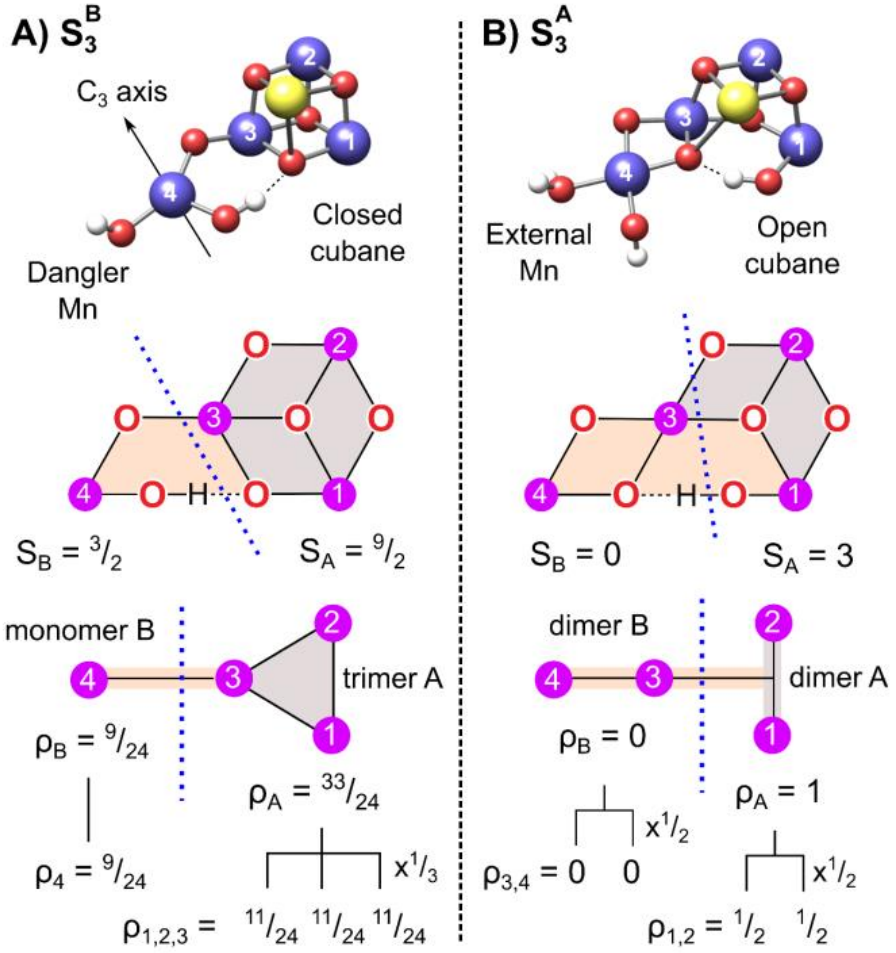

Figure S10 Density functional theory (DFT) structures developed for the S_3-state from the interconvertible S_2 state models described in Pantazis et al (18) **A)** closed cubane with five coordinate dangler Mn ion (19) and **B)** open cubane with additional water-derived ligand bound within the cubane (9). Below each mode is shown a 2D map of the exchange interactions between all four Mn ions. The grey shaded exchange pathways represent the ferromagnetic exchange interactions, whereas the orange shaded pathways represent the antiferromagnetic exchange interactions. These can be simplified into two idealized magnetic coupling topologies in which the spin system is decomposed into two spin fragments: **A)** a monomer-trimer (3 +1) coupling scheme and **B)** a dimer-of-dimers (2 + 2) coupling scheme. Spin projections for the two spin fragments and the resultant site spin projection coefficients for all four Mn ions are given, calculated using the **Eq. S10**.

i) When the Mn1-Mn3 coupling is F, i.e. the cofactor contains only one AF coupling, the topology can be described in terms of a trimer-monomer or 3 + 1 scheme, in which the Mn ions of the trimer are ferromagnetically coupled, while the monomer Mn ion is coupled to this unit antiferromagnetically. In this instance, we expect the three Mn ions which make up the trimer to carry the same spin projection (in terms of both sign and magnitude) and the fourth Mn ion to carry a similar spin projection but of opposite sign (**Fig. S10**).

ii) In contrast, when the Mn1-Mn3 coupling is AF, i.e. the cofactor contains two AF couplings, the topology can be described in terms of a dimer of dimers or 2 + 2 scheme, in which the complex can be considered as two distinct parts: Mn1 and Mn2 ferromagnetically couple to give an EPR active component, with each having large spin projection factors of the same sign, whereas Mn3 and Mn4 antiferromagnetically couple to give an EPR silent component, with each having small spin projection factors. Essentially, the second AF coupling counteracts the ferromagnetic interaction between Mn2 and Mn3. Note that the two descriptions above represent idealized coupling limits. A real system will fall somewhere in-between these two end points.

A dimer of dimers (2 + 2) topology best describes the untreated S_3 state (S_3^{Ca}) signal. This topology explains why the hyperfine tensors for this cofactor form fall into two groups, with two Mn transitions appearing at high frequency (strong coupling regime, A_1 and A_2) and two appear at low frequency (weak coupling regime, A_3 and A_4). As we will show, a trimer-monomer coupling topology is more compatible with the S_3' state as it displays four hyperfine couplings of similar magnitude.

Simulations of the EPR lineshape using the spin Hamiltonian formalism. An isotropic g-value of 1.99 and a spin state of $S = 3$ (as determined by microwave nutation experiments) were assumed for all simulations. As per our previous study (9), the untreated cofactor spectrum (S_3^{Ca}) can be explained by a single species. Spectral simulations reported here reproduce the zero-field splitting parameters (D, E/D), with the small D value characteristic of an exchange-coupled complex containing all octahedral Mn^{IV} ions. In the simulations reported here, we included the fourth-order zero-field splitting parameters a and F. These allowed the positions of all turning points of the S_3^{Ca} spectrum to be accurately reproduced (**Fig. 3**) to within 1 mT. In all perturbed samples examined in this study (S_3^{NH3}, S_3^{MeOH}, S_3^{Sr}) an S_3^{Ca} cofactor population was observed, which could be simulated using the same spin Hamiltonian parameters (see **Table S1**). The relative population of this S_3^{Ca} cofactor in modified preparations was estimated to be largest in the S_3^{NH3} sample (43%) and approximately the same in the S_3^{Sr} and S_3^{MeOH} samples (17-20% respectively). In the case of the S_3^{MeOH} sample, the S_3^{Ca} cofactor population could be modulated by changing the concentration of methanol (**Fig. S5**). However, at concentrations exceeding 5% v/v methanol, the cofactor started to decompose as evidenced by an increase in free Mn^{2+} concentration.

As stated in the main text, the S_3^{NH3}, S_3^{MeOH} and S_3^{Sr} all contain additional S_3 state signals. The S_3^{NH3} sample resolves a second S_3 state signal which is similar to the S_3^{Ca} cofactor signal in terms of both spectral width and structure. This new species is best resolved by examining the pseudo-modulated (CW/derivative-like) line shape (**Fig. 3, Fig. S11**). This is generated by convoluting the EPR spectrum with a Bessel function of the first kind. The second species is slightly broader; its spectral lines are best separated from the S_3^{Ca} cofactor signal on the high-field edge (see **Fig. S11**, marked with the asterisk and open triangle). Spin Hamiltonian parameters for this second

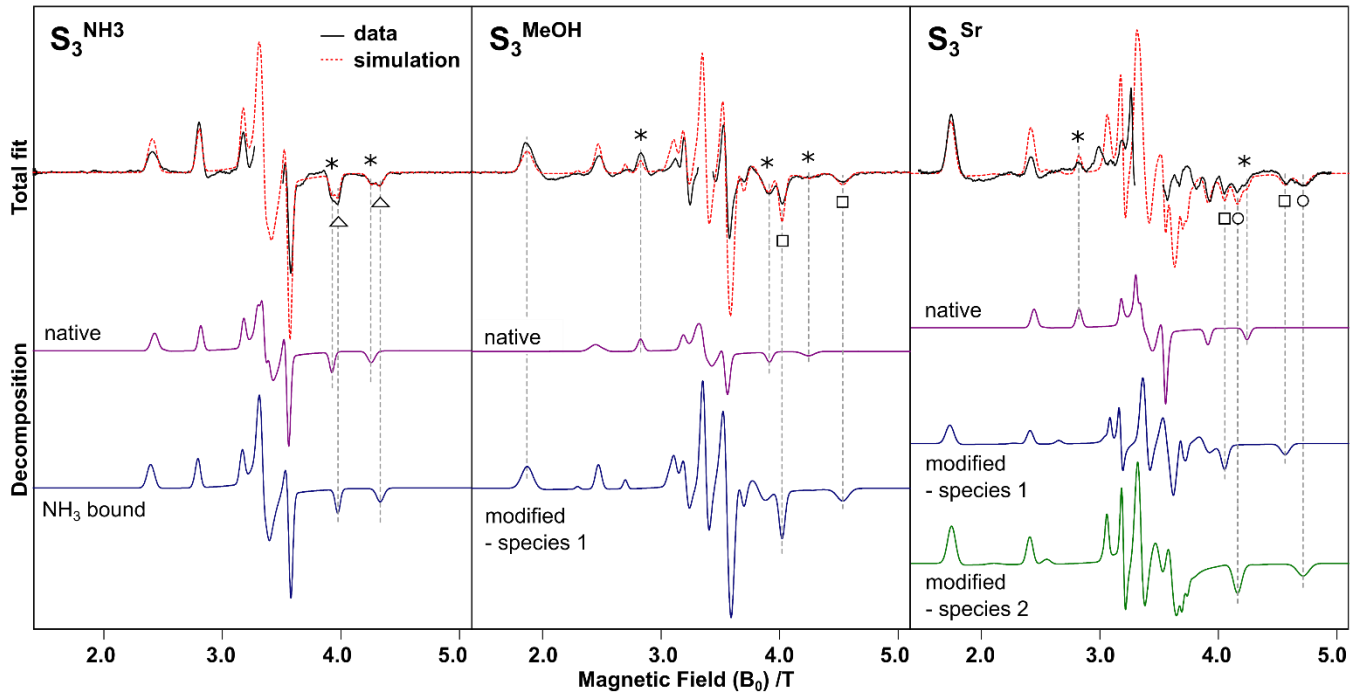

Figure S11: Simulation of the S_3-*minus*-S_1 spectra collected for the three investigated sample types: S_3^{NH3} - PSII with 100 mM NH_4Cl added, S_3^{MeOH} - PSII with 3% v/v methanol added and S_3^{Sr} - biosynthetically exchanged Ca^{2+}/Sr^{2+} PSII. The black traces represent the data, the red dashed traces represent the total simulated spectra. The latter is made up of at least two components, shown below. All simulations assume a total spin state of $S = 3$, an isotropic g value of 1.99, see **Eq. S5**.

population are systematically larger, with the D value increasing by about 5% (see **Table S1**). This modified S_3 state spectrum is still assigned to an exchange-coupled complex containing all octahedral Mn^{IV} ions. The second cofactor form presumably has the same structure as the S_3^{Ca} cofactor (S_3^A), with NH_3 bound to the cluster, i.e. to Mn4 (14, 15). An alternative assignment for this population is that it resembles another intermediate in the activation cycle, i.e. an S_3^B type structure in which proton shuffling between the two oxygen ligands on the Mn1-Mn4 axis is arrested (19-21).

The S_3^{MeOH} spectrum is also made up of two components of similar intensity. Here, however, the two components have very different spectral widths, and thus are easily distinguished. The narrow form (purple) is essentially the same as the untreated S_3 (S_3^{Ca}), whereas the broad form (blue) represents a new S_3 state form. The characteristic peaks of each component are marked by asterisks and open squares respectively. The spin Hamiltonian parameters for each component are listed in **Table S1**.

The fitted D value of the new S_3 cofactor form (S_3') is negative and approximately two-fold larger than that of the S_3^{Ca} cofactor signal (-0.28 *vs.* -0.17 cm^{-1}). The E/D value is lower indicating the system has increased axial symmetry (0.16 *vs.* 0.30). The inclusion of fourth-order terms are less important to reproduce spectral line positions. As stated in the main text, a D value in this range is consistent with an exchange-coupled complex which now contains a five-coordinate Mn ion, benchmarked against experimental data, specifically results collected on the S_2 state (22). A similar D value can also be calculated for a theoretical S_3' state model, in which the Mn4 ion is five-coordinate. In such models the local d calculated for Mn4 is estimated to be +2.14 cm^{-1} (e/d = 0.1) (19) using the L-CASCI methodology (23). A similar value (+2.5 cm^{-1}) has been observed in five-coordinate Mn^{IV} model complexes (24). Assuming a small d value of |0.3 cm^{-1}| for the other three octahedral Mn^{IV} ions and idealized estimated spin projection coefficients (3+1 scheme, ααaβ) (9), the total D is estimated to be <|0.34| cm^{-1}, in good agreement with the experimental value (see **Table S3**). Note that this earlier theoretical structure predicted a higher ground spin state of $S = 6$. This was due to the Mn3-Mn4 coupling pathway becoming weakly ferromagnetic. The magnitude of this coupling interaction however is within the error of the calculation, and thus a ground state of $S = 3$ for structures of this type is possible.

The S_3^{Sr} spectrum contains at least three components: a narrow form essentially the same as the untreated S_3 (S_3^{Ca}), and two broad forms (blue and green) that represent new S_3 state forms – at least two are needed to reproduce the structured central region and splitting on the high-field edge, reminiscent of the S_3^{NH3} fitting. The more axial broad form (blue) is very similar to that seen in the S_3^{MeOH} spectrum. The characteristic peaks of each component are marked by asterisks, open squares and open circles respectively. The spin Hamiltonian parameters for each component are listed in **Table S1**. The linewidth for each component was allowed to vary.

As before, the fitted D value of these new S_3 cofactor forms (S_3') is negative and approximately two-fold larger than the S_3^{Ca} cofactor signal (-0.30 *vs.* -0.17 cm^{-1}). The E/D values are, however, different, with one similar to the S_3^{MeOH} fitting (0.15), while the second (0.22) falls in-between that seen for S_3^{MeOH} and S_3^{Ca}. It is hypothesized that these two spectra represent the same cofactor structure seen for the S_3^{MeOH} sample, but which differ in terms of the precise structure of the first/second coordination sphere of the five coordinate Mn^{IV} ion (see mechanistic details section below).

W-band ^{55}Mn-EDNMR dataset. As described in the main text, double resonance methods such as EDNMR allow each Mn ion to be characterized in isolation. These data examine the magnetic (hyperfine) interaction between the unpaired electron(s) spin and the nuclear spin of each Mn ion. This interaction is dependent on the orientation of the cofactor relative to the applied magnetic field. We can access different orientations of the cofactor by performing the EDNMR experiment at multiple magnetic fields. This *2D*-EDNMR dataset then allows the complete hyperfine tensor of each ^{55}Mn nucleus to be experimentally determined.

The complexity of EDNMR spectra is due to the EPR spectrum being made up of six EPR transitions ($M_S \pm 1$). Of these only

the four lowest transitions significantly contribute to the EPR spectrum at cryogenic temperatures (5 K), **Fig. 3, S12**. Associated with each M_S level is a single NMR transition ($M_I \pm 1$). This NMR transition is observed in the EDNMR spectrum (**Fig. S12**), whose frequency is defined in the ***SI theory*** section above. Note that for the ^{55}Mn nucleus ($I = 5/2$) this is only true in the instance when the quadrupole coupling is smaller than the linewidth. As an EDNMR transition necessarily involves a transition between two different M_S and M_I levels, e.g. $|M_S \quad M_I\rangle \rightarrow |M_S + 1 \quad M_I + 1\rangle$, the EDNMR spectrum associated with each of the EPR transitions has two peaks (**Fig. S12**). In the following sections we will label these two peaks/contributions in terms of their M_S value only. Additional double quantum transitions can also be observed ($M_I \pm 2$) in some EDNMR spectra, when such a transition falls within the resonator bandwidth.

In our previous study on the final S_3^{Ca} state (9) the set of EDNMR spectra could be easily interpreted. The simplest EDNMR spectra are those that are measured on the edges of the EPR spectrum (2.6, 4.1 T), which is defined by a single EPR transition, the $M_S = |-3\rangle \rightarrow |-2\rangle$ transition (**Fig. 3, S12** blue component). At this position we would expect two peaks in the EDNMR spectrum for each ^{55}Mn nucleus: an NMR transition associated with the $M_S = |-3\rangle$ sub-manifold and an NMR transition associated with the $M_S = |-2\rangle$ sub-manifold.

The S_3^{Ca} EDNMR spectra measured at 2.6 and 4.1 T (**Fig. 4**) were interpreted as follows: the two doublets observed at ≈160 MHz (ν_α, ν_β) and ≈260 MHz (ν_α', ν_β') where assigned to two ^{55}Mn nuclei in the strong coupling limit ($|A| > 2\nu_L$). The position of the two peaks is defined as (**Fig. S12B**):

$$\nu_\alpha, \nu_\beta = 2|A_1| - \nu_L\,, 2|A_2| - \nu_L$$
$$\nu'_\alpha, \nu'_\beta = 3|A_1| - \nu_L\,, 3|A_2| - \nu_L \qquad \textbf{(Eqs. S14)}$$

Using the exact peak positions measured at either 2.6 T (ν_L = 27.4 MHz) or 4.1 T (ν_L = 43.2 MHz) yields the hyperfine coupling value (A_1 and A_2) of approximately -100 MHz. This result thus requires that the hyperfine tensors A_1 and A_2 be approximately isotropic as the EDNMR spectra recorded at these two magnetic field positions represent two completely different powder orientations.

In addition, a broader peak was observed between 20-40 MHz, close to the Larmor frequency in both the 2.6 and 4.1 T spectra (**Fig. 4**). This was assigned to the remaining two ^{55}Mn nuclei. Owing to the lack of structure of this peak, the hyperfine couplings A_3 and A_4 are less well defined, but clearly fall in the weak coupling limit ($|A| < 2\nu_L$). At more central positions within the EPR spectrum, the observed EDNMR spectrum is the superposition of multiple patterns, which can all be decomposed as above. Importantly, the interpretation described above holds at all positions as demonstrated by simultaneous fitting of the entire dataset.

A comparison between the S_3^{Ca} and S_3^{NH3} EDNMR spectra is shown in **Fig S13**. At all magnetic fields these two sample types resolve identical spectra suggesting the structure of the cofactor is the same for both sample types. However, as noted above, the S_3^{NH3} EPR spectrum contains a large proportion of the untreated (S_3^{Ca}) cofactor, which may conceal signals associated with the NH_3 bound population.

A similar comparison can be made between the S_3^{Ca} and the two modified S_3 state forms S_3^{Sr} and S_3^{MeOH} (**Figs S13-S14, S16)**. Here there are clear differences between the two sample types. As before, the simplest EDNMR spectra to interpret are those measured on the edges of the EPR spectrum (1.98, 4.4 T), which are defined by a single EPR transition, the $M_S = |-3\rangle \rightarrow |-2\rangle$ transition. As seen for the S_3^{Ca} EDNMR spectra, the two doublets are observed above 100 MHz. The positions of these doublets on the low-field edge (1.98 T, ν_L = 20.8 MHz) are: 160-175 MHz and 255–268 MHz, and on the high field edge (4.4 T, ν_L = 46.3 MHz): 145–158 MHz and 239–265 MHz. These correspond to two or more strongly coupled ^{55}Mn nuclei, similar to the S_3^{Ca} state, (for further details see the next section). These lines are expected to represent near-octahedral Mn^{IV} ions, as described in the main text.

In addition to these clustered transitions, both sharp and broad ^{55}Mn signals are also observed, whose spectral shape and position are strongly dependent on the magnetic field at which the EDNMR spectrum is measured. These include the sharp peaks seen between 20-80 MHz in the 1.98 T spectrum that are absent in the 4.4 T spectrum and broad lines that appear in the 4.4 T spectrum immediately before and underneath the 145-158 MHz peaks described above. Such signals cannot be ascribed to a single isotropic Mn^{IV} hyperfine tensor or a set of single isotropic Mn^{IV} hyperfine tensors. Thus these spectral features instead indicate at least one anisotropic ^{55}Mn hyperfine tensor that likely corresponds to a five-coordinate Mn^{IV} ion. This result is fully consistent with our EPR lineshape analysis which correlates an increase in *D* with the presence of a five coordinate Mn ion.

Unfortunately, as seen for the S_3^{NH3} EDNMR spectra, the untreated cofactor EDNMR signals are also observed particularly for spectra collected at the center of the EPR spectrum. If present, signals from the S_3^{Ca} cofactor will dominate the EDNMR spectrum because of its more favorable relaxation properties (slower T_1 and T_2). This can be readily seen by comparing EDNMR spectra measured in the range between 2.9 – 3.8 T of S_3^{Ca} and S_3^{MeOH} samples – they are essentially identical (see **Fig. S14**). As such, only EDNMR spectra collected at a magnetic field where the S_3^{Ca} cofactor signal is small can be analyzed.

Finally, it is also noted that only large ^{55}Mn-hyperfine couplings are clearly identified in modified S_3 state spectra (S_3^{MeOH}, S_3^{Sr}). The two weakly coupled ^{55}Mn nuclei seen in the set of S_3^{Ca} EDNMR spectra, which manifest as a broad peak near the ^{55}Mn Larmor frequency, have disappeared (9). This is taken as evidence that the spin topology of the cofactor *changes*. Specifically, these data require that all Mn ions carry a large spin projection coefficient. This implies that the electronic structure of the cofactor can be described in terms of the monomer-trimer coupling scheme, similar to that of the S_2^B state.

Simulations of the S_3^{MeOH} EDNMR dataset using the Spin Hamiltonian formalism. A brief description of the fitting procedure used to simulate the set of S_3^{MeOH} EDNMR data is given below. As alluded to above, only EDNMR spectra collected over the first and last thirds of the EPR spectrum could be included in the fitting owing to the overlap with S_3^{Ca} cofactor signals in the center of the EPR spectrum. This limited dataset is insufficient to independently constrain the four manganese hyperfine tensors and their relative orientations to each other and the *D* tensor. This can probably only be achieved through recourse to single crystal measurements. While this information is valuable, particularly for understanding precisely how the substrate waters bind to the cofactor and how proton release occurs, it is outside the scope of this study. However a unique fitting of the EDNMR dataset could be achieved by assuming all four Mn hyperfine tensors are collinear with the *D* tensor and axial, or near-axial in the case of Mn4. We also assumed that each has an equal integrated contribution to each EDNMR spectrum prior to correcting for resonator bandwidth. The

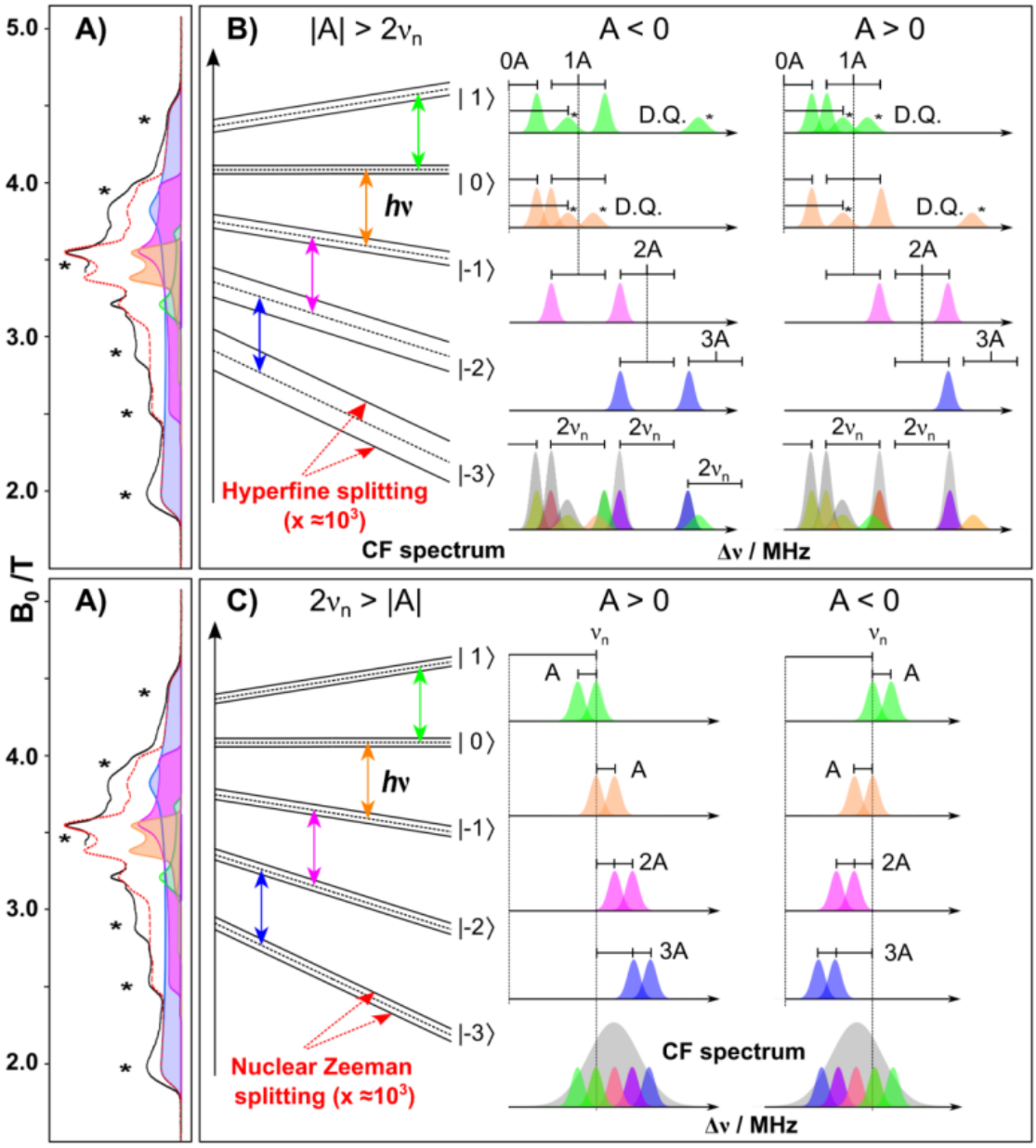

Figure S12. A) EPR spectrum of the S_3 state measured at W-band showing the positions (*) where the ^{55}Mn-EDNMR spectra were collected. **B)** Pictorial decomposition of nuclear transitions in the strong coupling limit associated with each EPR transition of the ground-state spin manifold: These appear at frequencies shifted by the ^{55}Mn nuclear Larmor frequency from multiples of the hyperfine coupling ($A \approx 100$ MHz) [$\nu_L(^{55}Mn) = 35.8$ MHz at 3.4 T]. The shifts are positive, e.g. for $M_S < 0$ and $A > 0$. The color of each nuclear spectrum matches the EPR transition with which they are associated. Asterisks mark "double-quantum" nuclear transitions. Because the hyperfine splitting in the spectra scales with the electronic M_S number, nuclear transitions associated with the $|-3\rangle \rightarrow |-2\rangle$) EPR transition define the high-frequency edge of the EDNMR spectra. **C)** Pictorial decomposition of nuclear transitions in the weak coupling limit associated with each EPR transition of the ground-state spin manifold. The spectra appear centered at the ^{55}Mn nuclear Larmor frequency and split by the hyperfine coupling. The composite center-field (CF) spectra shown at the bottom of (B) and (C) demonstrate the relative contributions of each transition to spectra measured in the center of the EPR spectrum.

Table S2: Fitted spin Hamiltonian hyperfine tensors ($\boldsymbol{A_i}$) for the EDNMR simulations in **Fig. 4**.

		Hyperfine tensor components[a] /MHz				
		A_x	A_y	A_z	A_{iso} [c]	A_{dip} [d]
S_3^{MeOH}	$\boldsymbol{A_1}$	-104.0	-104.0	-97.5*	-101.8	-2.2
	$\boldsymbol{A_2}$	-97.0	-102.5*	-97.0	-98.8	+1.8
	$\boldsymbol{A_3}$	-96.5	-96.5	-91.3*	-94.8	-1.8
	$\boldsymbol{A_4}$[e]	+28.0	+32.0	+127*	+62.3	+32.3
S_3^{Ca} [b]	$\boldsymbol{A_1}$	-97.9	-101.4	-97.8	-99.0	-1.2
	$\boldsymbol{A_2}$	-92	-98.9	-95.8	-95.6	+1.8
	$\boldsymbol{A_3}$	-	-	-	-25.9 or +7.0	-
	$\boldsymbol{A_4}$	-	-	-	< +5	-

[a] All hyperfine tensors were constrained to be collinear with the D tensor and axial (near axial in the case of A_4).
[b] Values taken from (9). Note that the value of A_3 depends on the assumed sign of the hyperfine coupling. It can take two discrete values, -26 MHz or +7 MHz and that the anisotropy for A_3 and A_4 hyperfine is not resolved from the fitted line width.
[c] The isotropic hyperfine value of each tensor is calculated as: $A_{iso} = [A_x + A_y + A_z]/3$.
[d] The dipolar component of each tensor is defined as: $A = A_{iso} + A_{dip}$ [-1 -1 +2], with the dipolar tensor coincident with the z-axis for A_1, A_2 and A_4 and with the y-axis for A_2 (unique tensor component marked with an *).
[e] When A_4 is constrained to be collinear with the D tensor, it is best described by a near-axial hyperfine tensor of very large anisotropy (A_{dip}), in which A_x and A_y are well defined and A_z is >125 MHz. If instead A_4 is allowed to rotate relative to the D tensor [10°, 20°, 0°], it is better described by a more rhombic hyperfine tensor [65.0, 30.0, 120.0], with larger A_{iso} (≈ 72 MHz) and smaller A_{dip} (24 MHz).

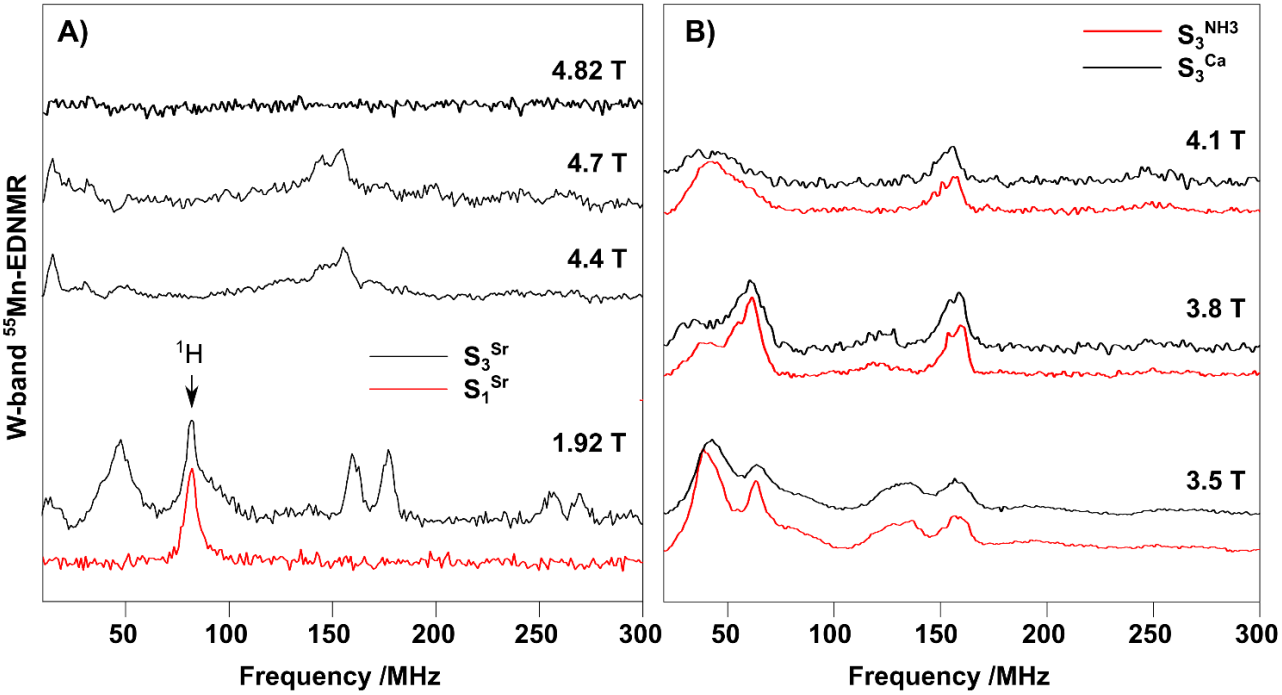

Figure S13. A) W-band ELDOR-detected NMR spectra at the low- (1.92 T) and high-field edge (4.4 – 4.7 T) of the S_3^{Sr} EPR spectrum. For magnetic field 1.92 T the S_1 spectrum (red) is also presented. The comparison between S_1 and S_3 makes clear which peaks are relevant to the S_3 state. The observed peaks are similar to those observed in the S_3^{MeOH} state. **B)** W-band ELDOR-detected NMR spectra of the S_3^{NH3} (red) in comparison with S_3^{Ca} (black) at three different magnetic field positions noted on the right.

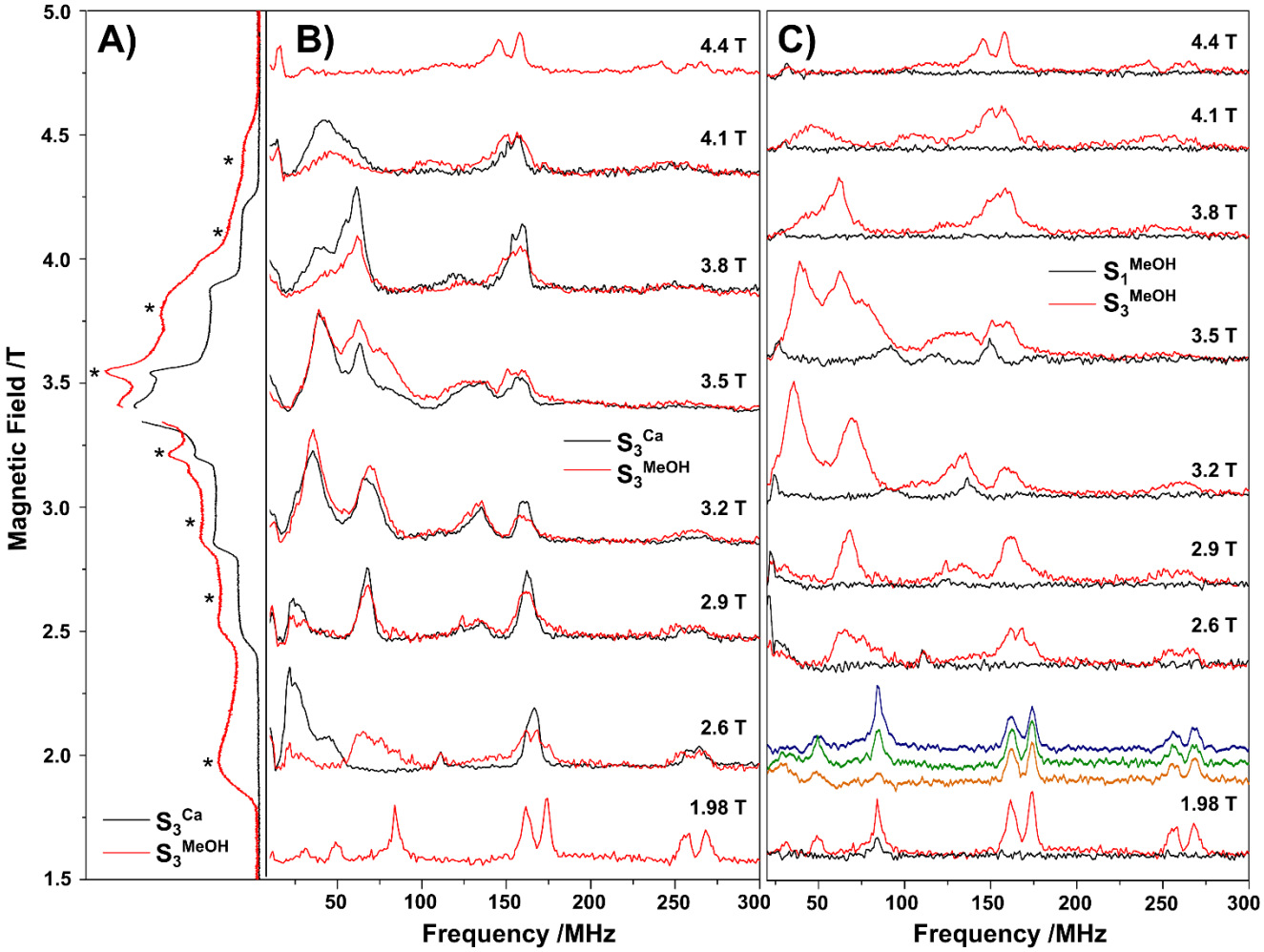

Figure S14. A) W-band ESE field-swept EPR of S_3^{Ca} (black) and S_3^{MeOH} (red) samples. EDNMR field positions are marked with asterisks. **B)** W-band ELDOR-detected NMR spectra of S_3^{MeOH} (red) in comparison with the S_3^{Ca} (black). **C)** W-band ELDOR-detected NMR spectra of S_3^{MeOH} (red) in comparison with the dark-adapted sample at S_1 (black). The field position of each spectrum is noted on the right. **Experimental parameters:** microwave power: 94.07 GHz; shot repetition rate: 0.5 ms; 320 points/spectrum; resolution ≈ 1 MHz; 1024 shots/point; 1.98 T ≈ 40 scans (S_3), 120 scans (S_1), 2.6 T - 3.8T ≈ 4-20 scans, 4.1 T ≈ 50 scans (S_3), 25 scans (S_1), 4.4 T ≈ 240 scans (S_3), 140 scans (S_1); temperature: 4.8 K. Additional colored EDNMR traces collected at 1.98 T using three different power values for the HTA pulse (6, 12 and 18 dB) are also shown. These data clearly identify the ^{55}Mn peaks, which do not change with HTA pulse amplitude, as compared to ^{1}H, and transitions around 50 MHz which are associated with spin forbidden EPR transitions.

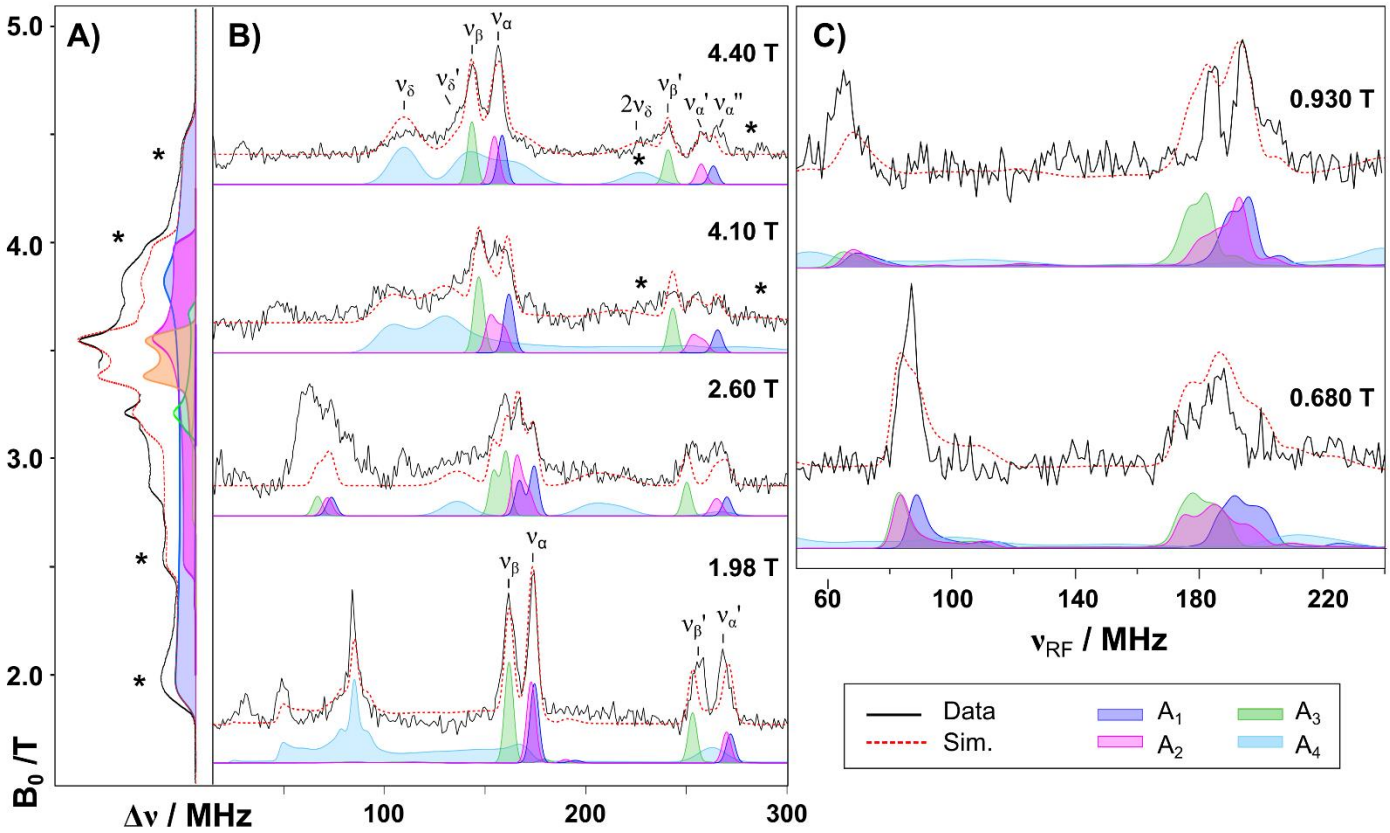

Figure S15: **A)** Experimental (black) and simulated (red) W-band EPR spectrum of the modified S_3 state (S_3^{MeOH}). The deconvolution of the simulation to the EPR transitions is also shown (see **Fig. 3**). Asterisks indicate the positions where EDNMR spectra were recorded; **B, C)** Spin Hamiltonian simulations of W-band EDNMR spectra (1.98, 2.60, 4.10 and 4.40 T) and Q-band ENDOR spectra (0.68 and 0.93 T) used to constrain the four ^{55}Mn hyperfine tensors. Residual S_3^{Ca} signals in the EDNMR spectra collected at 2.60, 4.10 T were suppressed by a scaled subtraction of the corresponding S_3^{Ca} EDNMR spectrum. Experimental data are shown as black lines, simulations as red dashed lines. A decomposition of the fitting into individual ^{55}Mn nuclei (A_1-A_4) is also shown (see color code). Simulation parameters are listed in **table S2**. To minimize the set of independent variables in our simulation we assumed all four ^{55}Mn hyperfine tensors are collinear with the *D* tensor and axial, or near-axial in the case of Mn4 and that each has an equal integrated contribution to each EDNMR spectrum prior to correcting for resonator bandwidth. The inclusion of the quadrupole interaction did not improve the simulations.

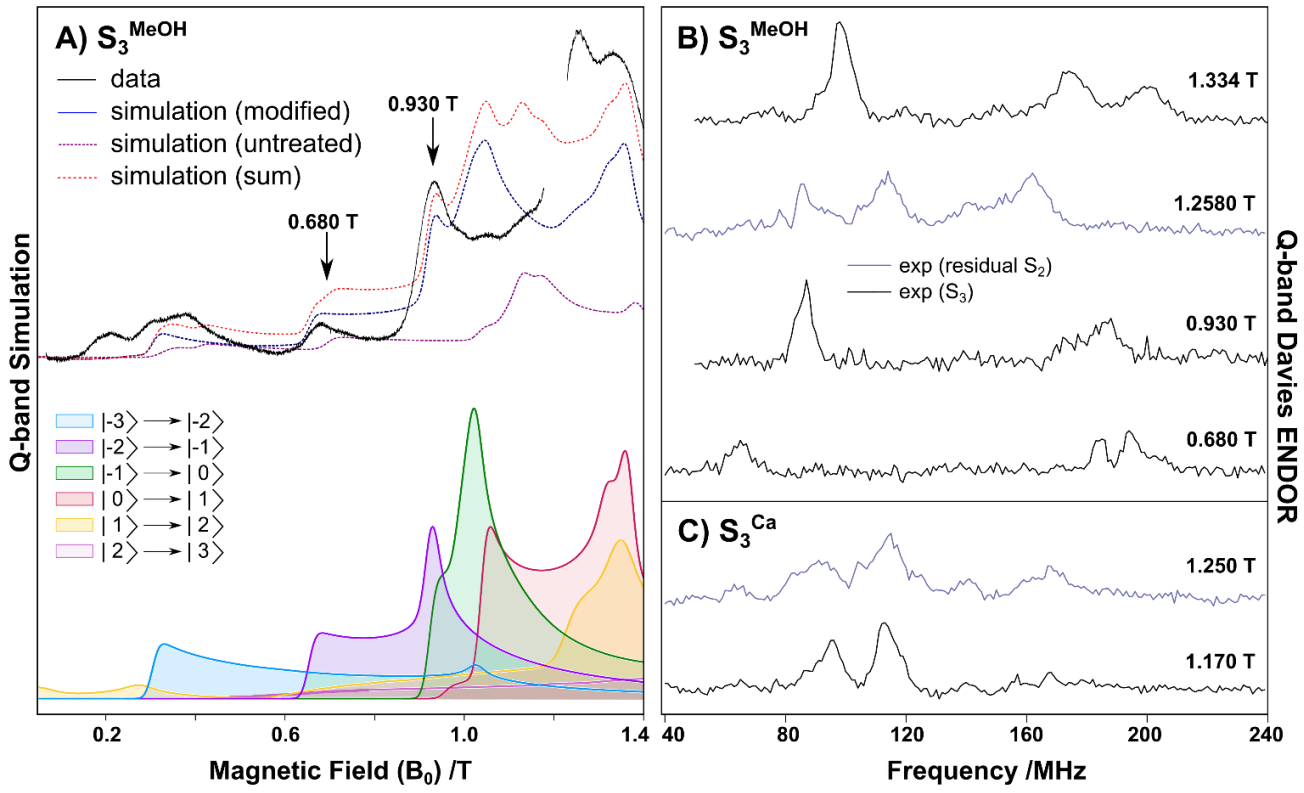

Figure S16. **A)** Experimental (black) and simulated (red dotted) EPR spectra of the methanol-treated S_3 state at Q-band. The red dotted spectrum is the sum of the untreated S_3 spectrum (purple dotted spectrum) and a broader component (blue dotted). The simulation parameters are the same as for **Fig. S11** (middle). On the bottom the deconvolution of the broad S_3 spectrum to the EPR transitions populated at this temperature is shown. **B)** Q-band pulse ^{55}Mn-Davies ENDOR of the S_3^{MeOH}. **C)** Q-band pulse ^{55}Mn-Davies ENDOR of the S_3^{Ca}. In panel B and C the residual S_2 signal at ≈ 1.25 T is depicted in blue. **Experimental parameters:** microwave frequency: 34 GHz; shot repetition time: 0.5 ms; microwave pulse length (t_p): 10 ns; τ: 242 ns; radio frequency pulse (t_{RF}): 3.5 µs; temperature: 7 K.

inclusion of the quadrupole interaction did not improve the simulations.

There is a solid structural basis as to why the four Mn hyperfine tensors of the cofactor should be collinear. The cofactor resembles a distorted chair (**Fig. 1**) with the base of the chair (cubane unit) made up by the three Mn ions Mn1, Mn2 and Mn3. As the name suggests, the cubane unit resembles a cube with three of the vertices being Mn, one Ca and the remaining four bridging oxygens. Apart from the Ca vertex, which owing to the longer Ca-O bonds is drawn out of the cube, the other corners of the cube (Mn1, Mn2, M3, O1, O2 and O3) are undistorted, with all Mn-O bond lengths similar. A series of bridging carboxylates ligands between Mn1-Mn2 and Mn2-Mn3 also enforce the cubic symmetry. As such, we would expect the ^{55}Mn hyperfine tensors to be either aligned or rotated 90° to each other. This is the case for heterometallic Mn_3O_4Ca cubane complexes which mimic this structural element of the cofactor (25). The fourth Mn ion (Mn4), as it is not part of the cubane unit, is the one Mn that is most likely to have a non-collinear Mn tensor. It is still connected to the cubane unit via oxygen bridge linkages (O4), forming the back of the so called distorted chair. As such, while it may not have exactly the same coordinate frame, it should be similar, with at least one axis coincident with the Mn ions of the cubane unit. This high level of symmetry should then also lead to the *D* tensor being collinear, or near collinear to the set of four Mn tensors, as the principal axis of each of the site *d* (zero-field) tensors should align with the principal axis of the site *a* (hyperfine) tensors.

Four W-band EDNMR spectra (1.98, 2.60, 4.10 and 4.40 T) and two Q-band ENDOR spectra (0.68 and 0.93 T) were included in the fitted dataset. For the EDNMR spectra collected at 2.60, 4.10 T residual S_3^{Ca} signals were suppressed by a scaled subtraction of the corresponding S_3^{Ca} EDNMR spectrum.

Starting with the low-field EDNMR spectrum recorded at 1.98 T, which is derived from the $|-3\rangle \rightarrow |-2\rangle$) EPR transition (**Fig. S12** blue component): two transitions are observed at 162 (ν_β) and 174 MHz (ν_α) together with their related partner lines at 256 MHz (ν_β') and 268 MHz (ν_α'), see **Fig. S15**. Simulation of these lines requires the inclusion of two hyperfine tensors (A_1 and A_3). ν_α and ν_β are seen at similar positions at all magnetic fields demonstrating that the hyperfine tensors that describe them are approximately isotropic. The line positions match the following condition:

$$\nu_\alpha, \nu_\beta = 2|A_1| - \nu_L\,, 2|A_3| - \nu_L$$
$$\nu'_\alpha, \nu'_\beta = 3|A_1| - \nu_L\,, 3|A_3| - \nu_L \qquad \textbf{(Eqs. S14)}$$

Requiring A_1 and A_3 to be negative. The intensity of ν_α relative to the ν_β measured at 1.98 T suggests that it is made up of two NMR transitions. Consistent with this observation, this transition appears broader when measured on the high field edge (at 4.4 T, ν_α = 158 MHz) and its partner line in the high frequency region splits into two lines e.g. 258 (ν_α') and 265 (ν_α'') MHz (**Fig. S14**). To reproduce this observation a further hyperfine tensor (A_2) needed to be included in the simulation. Thus the sharp features of the EDNMR spectra above 100 MHz are indicative of three, near isotropic hyperfine tensors (A_1, A_2, A_3), with two of them near-identical and symmetry–related, i.e. the magnitudes of A_1 and A_2 are approximately the same, but their tensor components are interchanged ([-104 -104 -97.5] vs. [-97.0 -102.5 -97.0], consistent with the two tensors being rotated by 90° to each other, as could be expected for a cubane like structure (**Fig. S15**).

In addition to these three hyperfine tensors a fourth, more anisotropic hyperfine tensor (A_4) is needed to model the broad EDNMR lines observed between 100-170 MHz at all magnetic fields, with the possible exception of 1.98 T. As we discuss below, this fourth tensor also explains the sharp lines between 20 to 80 MHz in the EDNMR spectrum recorded at 1.98 T. Starting now with the high-field EDNMR spectrum recorded at 4.4 T, which is derived from the $|-3\rangle \rightarrow |-2\rangle$) EPR transition: two broad transitions are observed at ≈112 (ν_δ) and between 140-150 MHz (ν_δ'), see **Fig. S15.** Note the double frequency $2\nu_\delta$ seen around 230 MHz (and possibly $2\nu_\delta$') both representing double quantum transitions (*) are also observed (**Fig. S15**). However, unlike the sharp EDNMR features, the positions of ν_δ and ν_δ' shift significantly on moving from the high-field edge to the low-field edge, demonstrating the tensor is anisotropic. The positions of the single quantum lines seen at 4.1 and 4.4 T EDNMR spectra match the following condition:

$$\nu_\delta = 2|A_4| + \nu_L$$
$$\nu'_\delta = 3|A_4| + \nu_L \qquad \textbf{(Eqs. S15)}$$

Requiring A_4 to be ***positive*** with the hyperfine component visualized on the high-field edge ($A_{4,X}$ and/or $A_{4,Y}$) being of the order of +30 MHz (see **Fig. S14, panel B** and **Fig. S15**). The corresponding hyperfine component visualized on the low-field edge ($A_{4,Z}$) is not well defined lying outside of the bandwidth of the resonator and as such is weak. Simulations of the entire dataset suggest it is of the order of +130 MHz, as this value best reproduces how the broad signal changes when moving from low field (2.6 T) to high field (4.1 and 4.4 T), see **Fig. S15**.

Finally, we note that two different linewidths needed to be used to simulate the set of W-band EDNMR and Q-band ENDOR spectra. A narrow linewidth of 5 MHz was used for the set of three near-isotropic hyperfine tensors (A_1, A_2 and A_3) and a broader linewidth of 15 MHz was used for the fourth, more anisotropic hyperfine tensor (A_4). This result intuitively makes sense. The three near-octahedral Mn^{IV} ions should display negligible quadrupole coupling, which would manifest here as broadening, owing to the near-spherical electron density of the half-filled t_{2g} orbital set and thus appear narrow. The same result was observed for the untreated S_3 (S_3^{Ca}) cofactor. The fourth anisotropic hyperfine tensor is instead indicative of a less symmetric Mn^{IV} ion. This should have a quadrupole contribution to its linewidth. Similarly, we suspect a higher degree of heterogeneity associated with the less symmetric Mn^{IV} ion. In our preferred model for the S_3' state discussed below, the less symmetric Mn ion is the outer Mn ion (Mn4) which has a highly flexible ligand field, with calculations suggesting its two water derived ligands being able to pivot around the Mn4/Glu333/Asp170 axis (19). This heterogeneity should manifest in terms of hyperfine strain and thus the dynamic nature of this Mn site is encoded in its apparent linewidth.

Sharp transitions between 20-80 MHz observed in the EDNMR spectrum recorded at 1.98 T provide further evidence for an anisotropic Mn hyperfine tensor (A_4). The EDNMR spectrum recorded at 1.98 T contains contributions from weakly allowed EPR transitions of the spin manifold, i.e. transitions in which the M_S value changes by more than ±1. This is shown in the **Fig. S9**. Note: accounting for weakly allowed EPR transition only needs to be considered for EDNMR spectra recorded at small magnetic fields <2 T. At higher magnetic fields the S_3^{MeOH} cofactor moves into the strong field regime and as such only spin allowed EPR transitions are observed. Similarly, these transitions are not present in EDNMR recorded for S_3^{Ca} as its EPR spectrum is much narrower (**Fig. S9**).

An analysis of the powder pattern contributions to the S_3^{MeOH} EPR signal recorded at 1.98T reveals that the allowed $|-3\rangle \rightarrow |-2\rangle$ transition only makes up ≈75% of the observed spin echo.

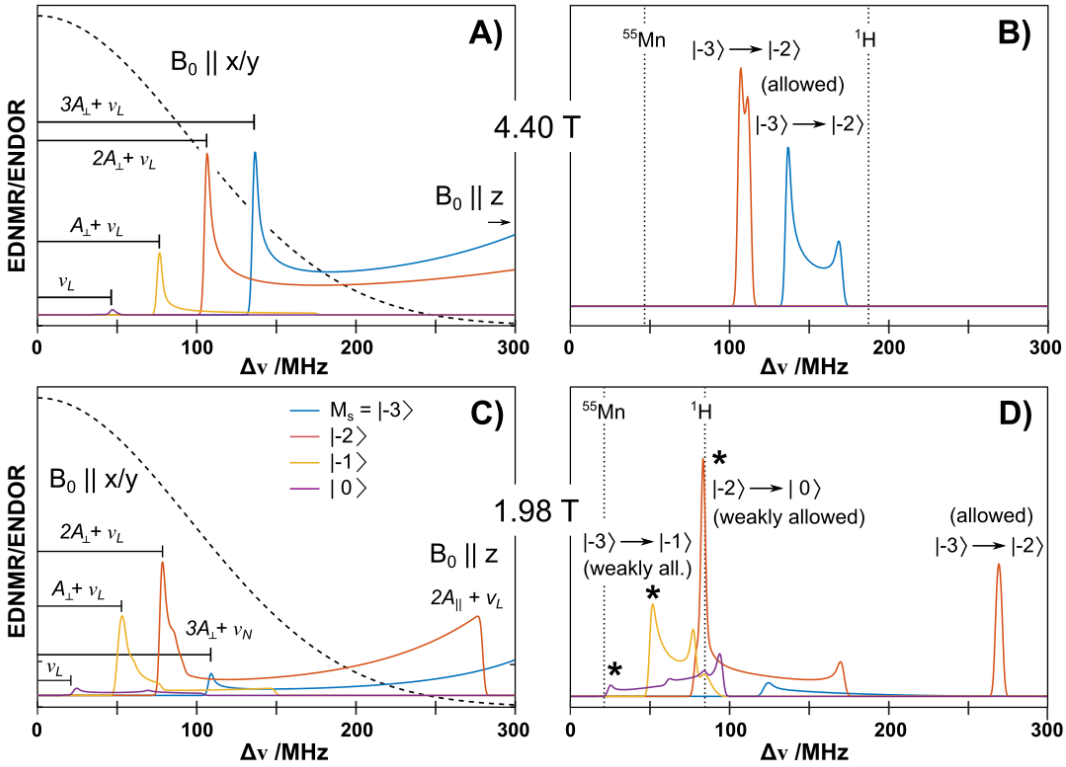

Figure S17. Simulation of the anisotropic ^{55}Mn hyperfine tensor (A_4) component of the experimental EDNMR spectra. The simulation assumes an axial hyperfine tensor of the form A = [+30+ 30 +130] MHz. Panels **A** and **C** show the complete NMR spectrum of each M_S level at 1.98 T (**C**) and 4.4 T (**A**) and assuming the measurement temperature is 4.8 K. Panels **B** and **D** show the same simulation including orientation selection and taking into account the resonator bandwidth (dashed line in panels **A** and **C**). This simulation qualitatively reproduces the sharp low-frequency lines seen in the 1.98 T EDNMR spectrum, which are visualized via the weakly allowed M_S $|-3\rangle \rightarrow |-1\rangle$ and $|-2\rangle \rightarrow |0\rangle$ transitions and the broad lines seen between 100-170 MHz in the 4.4 T EDNMR spectrum which are visualized via the allowed M_S $|-3\rangle \rightarrow |-2\rangle$ transition.

Table S3: Calculated site spin Hamiltonian parameters for the S_3^{MeOH} and S_3^{Ca} forms of the S_3 state

Spin projection coefficients									
Model	*topology*	Mn_1		Mn_2		Mn_3		Mn_4	
		ρ_1	κ_1	ρ_2	κ_2	ρ_3	κ_3	ρ_4	κ_4
3 + 1	αααβ	0.46	0.15	0.46	0.15	0.46	0.15	-0.38	0.08
2 + 2	αααβ	0.50	0.20	0.50	0.20	0.00	0.00	0.00	0.00
$S_3^{Aa)}$	αααβ	0.48	0.18	0.44	0.13	0.18	-0.02	-0.11	-0.03

Fitted hyperfine couplings A_i /MHz								
	A_1		A_2		A_3		A_4	
	iso	*dip*	*iso*	*dip*	*iso*	*dip*	*iso*	*Dip*
S_3^{MeOH}	-101.8	-2.2	-98.8	+1.8	-94.8	-1.8	+62.3	+32.3
S_3^{Ca}	-99.0	-1.2	-95.6	+1.8	-25.9[b)]	[c)]	<5	[c)]

Estimated site hyperfine couplings a_i /MHz[d)]								
	a_1		a_2		a_3		a_4	
	iso	*dip*	*iso*	*dip*	*iso*	*dip*	*iso*	*Dip*
S_3^{MeOH} (3 + 1)	-222	-4.8	-216	+2.2	-207	-3.8	-166[e)]	-86
S_3^{Ca} (2 + 2)	-198	-2.4	-191	+3.6	-	-	-	-

Estimated fine structure parameter $\|d\|$ /cm^{-1}			
	$\|d\|$	$\|D\|$[i)]	*Exp.*
S_3^{MeOH} (3 + 1)	$d_1, d_2, d_3, \leq 0.3$,[f)] d_4 = 2.3[g)]-2.5[h)]	≤0.34	0.281
S_3^{Ca} (2 + 2)	$d_1, d_2, d_3, d_4 \leq 0.3$	≤0.12	0.175

[a)] Spin projection estimates from broken symmetry DFT calculations of the final S_3 state (9)
[b)] The value of A_3 depends on the assumed sign of the hyperfine coupling. It can take two discrete values, -26 MHz or +7 MHz (9)
[c)] The A_3 and A_4 hyperfine couplings are assumed to be isotropic. The anisotropy is not resolved from the fitted linewidth
[d)] Site hyperfine estimates made by multiplying the experimental value by $1/\rho_i$ assuming a 2+2 model for S_3^{Ca} and a 3 + 1 model for S_3^{MeOH}. Site hyperfine values are all negative, as expected and fall within the -180 to -250 MHz range (see footnote e)
[e)] a_4 falls just outside the expected range when assuming the hyperfine tensor collinear with the D tensor (24). If this condition is relaxed a_4 decrease to ≈-190 MHz
[f)] Range seen in octahedral, monomeric Mn^{IV} model complexes i.e. $d \leq h\nu$, where ν = 9 GHz (X-band).
[g)] Theoretical value reported for the five-coordinate site in the S_3' model of Retegan et al. (19)
[g)] Experimental value recently reported for a trigonal bipyramidal Mn^{IV} model complex (24).
[i)] Assuming the four Mn^{IV} ions all have an identical site fine structure value (0.3 cm^{-1}), all d_i and κ_i values are positive and that all four onsite fine structure tensors are collinear.

There are also contributions from the $|-3\rangle \rightarrow |-1\rangle$ and $|-2\rangle \rightarrow |0\rangle$ transitions. As such, we expect an EDNMR signal associated with all these M_S levels, i.e. we would expect to see transitions at approximately ν_L, ν_L + A, ν_L + 2A. Assuming a positive hyperfine of A = +30 MHz (i.e. the x, y component of A_4, see above) yields EDNMR transition frequencies of:

$$|-2\rangle \rightarrow |0\rangle \;\Rightarrow\; \nu_L \approx 20.8\,MHz,\; \nu_L + 2A \approx 80.8\,MHz$$
$$|-3\rangle \rightarrow |-1\rangle \;\Rightarrow\; \nu_L + A \approx 50.8\,MHz$$

This set of sharp signals are clearly observed in the 1.98 T EDNMR spectrum, with the last one being coincident with the ^{1}H line (ν_H = 84.3 MHz). Note in the instance of a broad signal, indicative of an anisotropic hyperfine tensor, these values represent the edges of the signal profile with the precise positions of peaks dependent on orientation selection, e.g. this leads to the low frequency line shifting to about 30 MHz, (see **Fig. S17, panel D**).

The question that arises is why these transitions are not superimposed by more intense EDNMR lines associated with the allowed EPR transition, specifically a line at $\nu_L + 3A$ (110.8 MHz)? The suppression of this line can be considered strong evidence that the hyperfine tensor (A_4) that describes these transitions is anisotropic.

The spin allowed and weakly allowed transitions that define the EPR signal on the low-field edge are derived from completely different powder pattern orientations: the allowed $|-3\rangle \rightarrow |-2\rangle$ transition is on-resonance for a powder pattern orientation aligned with the z-axis, whereas the weakly allowed $|-3\rangle \rightarrow |-1\rangle$ and $|-2\rangle \rightarrow |0\rangle$ transitions are instead on-resonance for a powder pattern orientation aligned with the y-axis. This has the consequence that the two transition types select out different components of the hyperfine tensor: the $|-3\rangle \rightarrow |-2\rangle$ transition visualizes the $A_{4,Z}$ component, while the $|-3\rangle \rightarrow |-1\rangle$ and $|-2\rangle \rightarrow |0\rangle$ transitions instead visualize the $A_{4,Y}$ component. Thus if the $A_{4,Z}$ component is significantly larger than that of $A_{4,Y}$, the $\nu_L + 3A$ line is spread to higher frequencies and suppressed relative to the $\nu_L + A$ (50 MHz) and $\nu_L + 2A$ (80 MHz) line. This is shown in the **Fig. S17**.

The simulation shown in **Fig S17** assumes an axial hyperfine tensor of the form A_4 = [+30 +30 +130] MHz. The left-hand side of the figure plots the complete NMR spectrum associated with each M_S level at both 1.98 T and 4.4 T, assuming a measurement temperature of 4.8 K. The perpendicular components ($A_{4\perp}$ = $A_{4,X}$, $A_{4,Y}$) define the low-frequency edge, while the parallel (unique) component ($A_{\parallel}$ = A_{4Z}) defines the high-frequency edge. The right-hand side of the figure shows the same simulation including orientation selection and taking into account the resonator bandwidth. It can be readily seen that NMR transitions within the $M_S = |0\rangle, |-1\rangle, |-2\rangle$ levels readily explain the sharp spectral features seen in the EDNMR spectrum measured at 1.98 T, which are visualized via the weakly allowed $|-3\rangle \rightarrow |-1\rangle$ and $|-2\rangle \rightarrow |0\rangle$ transitions and the broader transition seen on the high field edge visualized by the allowed $|-3\rangle \rightarrow |-2\rangle$ transition. In the full simulation shown in **Fig. S15** a line width of 5 MHz was assumed for these transitions and their intensity, relative to signals derived from the other three nuclei enhanced by a factor of 2-4.

As a final note, we suspect there is also a double quantum ^{14}N EDNMR transition in the 20-30 MHz region (**Fig. 4, S14-S15**). This signal comes from the ^{14}N histidine ligand of Mn1. The inferred magnitude of the hyperfine interaction ($A(^{14}N)$ = 3 MHz) matches the value measured for this ligand in the preceding S_2 state, accounting for the change in spin projection factors, i.e. the spin projection factors should change from about 1.5 in S_2 to about 0.45 in S_3 owing to the change in the total spin of the complex.

The anisotropic tensor (A_4) is consistent with a trigonal bipyramidal (TBP) Mn^{IV} ion. TBP complexes recently characterized by the Borovik laboratory (24) display an anisotropic hyperfine tensor where the unique tensor component (A_Z) is largest in absolute magnitude. These same properties are seen for the anisotropic hyperfine tensor (A_4) in our simulation. Furthermore, the magnitude of A_4 is also similar to that seen for these model complexes. To make this comparison we first need to convert A_4 to the corresponding site hyperfine tensor (a_4). This is achieved by multiplying the fitted tensor by the inverse of the spin projection factor associated with Mn4. This site hyperfine tensor (a_4, **Table S3**) has an isotropic hyperfine component (a_{iso}) that is negative and of the order of -166 MHz, which is slightly smaller than that of the Borovik model (-199 MHz, or within 16%).

We note that in our simulations we forced all tensors to be collinear to reduce the parameter set. We suspect however that A_4 is rotated relative to the *D*-frame. Indeed, in the Borovik model complex the hyperfine tensor needed to be rotated by 36° relative to *D* about *y* to reproduce the EPR spectrum. In additional simulations (not shown), in which we allowed A_4 to rotate relative to *D*, the isotropic component of the tensor decreases to ≈-190 MHz, in good agreement with the Borovik model, see **Table S3.**

S_3^{MeOH} EDNMR is only consistent with a 3+1 coupling topology. Our EPR/EDNMR simulations provide strong evidence that the cofactor has a similar electronic structure to that of the precursor S_2^B state. As described above, in order to simulate the set of EDNMR/ENDOR spectra, three similar negative hyperfine tensors and one positive hyperfine tensor needed to be included. As the site hyperfine tensor associated with each ^{55}Mn nucleus is expected to be negative, this implies that the magnetic topology of the cofactor can be described in terms of a set of three positive and one negative spin projection factors, i.e. three of the Mn ion carry α spin and one carries β spin. As described above, this set of spin projection factors describes a 'monomer-trimer' or '3+1' coupling topology. This comes about when three of the Mn ions are coupled ferromagnetically, as they are in a heterobimetallic cubane (trimer unit: Mn1, Mn2, Mn3), which is then coupled antiferromagnetically to a dangler Mn ion (monomer unit: Mn4), as is seen for the S_2^B state. The hyperfine anisotropy also allows us to assign the coordination number of each Mn ion. The three negative hyperfine tensors, assigned to the Mn of the heterobimetallic cubane, all display small anisotropy consistent with six-coordinated Mn ions. In contrast, the positive hyperfine tensor has a large anisotropy consistent instead with a five-coordinated Mn ion. Thus our combined EPR/EDNMR/ENDOR results suggest that the S_3' cofactor represents a heterobimetallic cubane (Mn_3O_4Ca) tethered to a five-coordinate Mn ion, as proposed earlier in (19).

Earlier evidence of modified S_3 state EPR signals. Earlier observations reported in the literature for the S_3 state are consistent with the high-field EPR spectra shown here. Using standard X-band EPR (perpendicular mode) the untreated S_3 state spectrum is difficult to resolve, with only one clear turning point at approximately g ≈ 10 (26). The addition of methanol and also high levels of glycerol (50% v/v) was shown to diminish this marker signal with no other signal appearing in its place. At X-band, the methanol-induced modified S_3 state signal reported here would not be observed as the *D* value is approximately the same size as the microwave quantum at X-

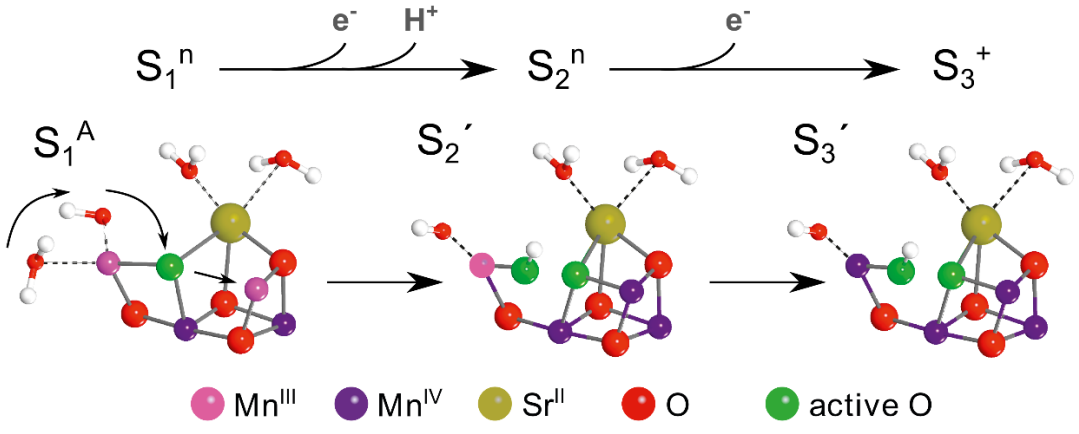

Figure S18. Proposed S_2 to S_3 state transition for the Mn_4O_5Sr cofactor.

band (9 GHz, 0.3 cm^{-1}), explaining this earlier result. Similarly, the addition of NH_3 was seen to lead to a small shift of the $g \approx 10$ marker signal (27). This too is consistent with our high-field data which shows that ammonia affects only 50% of the PSII centers and its effect on this 50% is subtle. We do, however, note that a recent low-frequency (X-band) report of biosynthetically modified *T. elongatus* (Ca^{2+}/Sr^{2+} exchange) did not resolve a change in the EPR spectrum from wild type (28). Our high-field measurements on the PSII-Sr sample does contain some wild type component, so a $g \approx 10$ signal is still expected to be observed, but as with the methanol addition, at a lower level. As its intensity was not rigorously quantified, we must assume this previous study was only observing the fraction of centers that exhibit a wild-type like S_3 cofactor form. We also hasten to point out that at X-band this region contains other spectral marker (Fe^{3+} signals from high-spin cytochromes and the non-heme iron site). While our results are consistent with these earlier observations, our spectral fittings do differ. An earlier X/Q-band EPR study of the methanol-treated PSII interpreted the modified S_3 state as $S = 3$ spin state with $D \approx 0.8$ cm^{-1}, a much higher value than that deduced here. This, however, was based on simulation of a single turning point, whereas at high field the whole spectrum can be resolved. We also note that in the earlier study PSII from spinach was used. It has been recently shown that methanol has greater access to the Mn_4O_5Ca cofactor in spinach preparations, which may lead to somewhat different zero-field splitting parameters (17).

Mechanistic details: the $S_2 \rightarrow S_3$ transition. In this manuscript we show clear evidence that the S_2 to S_3 transition is multistep and for the first-time outline bio/chemical methods to capture intermediate states, by low-temperature trapping. The perturbations introduced are not inhibitory, allowing the catalysis to advance to the final S_3 state. Equally however, small molecules and Ca^{2+}/Sr^{2+} exchange alter the energy landscape describing the S_2 to S_3 transition, introducing barriers of sufficient magnitude to allow intermediate populations to be characterized. This presumably explains the slowed reaction kinetics for the O-O bond formation associated with these treatments.

As stated in the main text, kinetic arguments can be made to explain how methanol could hinder water delivery to the cofactor, via water channels that lead to Mn4. Presumably methanol competes with water binding to the cofactor (although it does not directly bind to a Mn site) or potentially perturbs the H-bonding network/protein conformation near the site of water binding. This will shift the equilibrium populations of the S_3 state with and without an additional bound water molecule. A similar argument can be made to explain the same phenomenology observed for the Ca^{2+}/Sr^{2+} exchanged cofactor. Here we suspect altered proton release, which is coupled to S_2 to S_3 progression, could change the equilibrium populations of the S_3 state with and without an additional bound water molecule. Specifically, recent data has shown that Ca/Sr exchange changes the pK_a's of the cofactors titratable ligands (W1, W2) (28). As cofactor deprotonation via W1 to Asp61 is considered the pathway for proton egress – with Asp61 acting as a gate, changing this acid/base couple could influence water binding.

One hypothesis is that in PSII in which Ca^{2+} is replaced with Sr^{2+}, the deprotonation step associated with the $S_2 \rightarrow S_3$ transition occurs one step earlier, i.e. in the $S_1 \rightarrow S_2$ transition (**Fig. S18**). This could potentially lead to a decoupling of cofactor deprotonation from the water binding/delivery step. Evidence for this comes from the observation that PSII-Sr exhibits an altered high-spin S_2 state EPR signal when flash advanced. This signal, centered at $g \approx 5$, requires the E/D of the cofactor to collapse (1, 28). As the D and E values of the cofactor in the S_2 state are mainly representative of the only Mn^{III} ion, for the reasons given above, this S_2 state signal may indicate that the ligand field of the Mn4 is different from that in wild type. We note that trigonal bipyramidal Mn^{III} models display small E/D values. If cofactor deprotonation can occur in the S_2 state, presumably via the Asp61, the hydrogen bonding network that keeps Mn4 square pyramidal as opposed to trigonal bipyramidal would be lost (19). This could then lead to a spontaneous ligand field rearrangement explaining the modified S_2 state EPR signal. It may also explain changes in the FTIR difference spectrum associated with water bound at the Ca^{2+}/Sr^{2+} site (29). Thus the Aps61 gate does not function as intended in the S_2 to S_3 transition, possibly taking multiple conformations, some of which, together with local H-bonding preferences, may exclude water binding at Mn4. This may explain why the S_3 state in Ca^{2+}/Sr^{2+} exchanged samples is heterogeneous.

SI References

1. Boussac A, *et al.* (2004) Biosynthetic Ca^{2+}/Sr^{2+} exchange in the photosystem II oxygen-evolving enzyme of *Thermosynechococcus elongatus*. *J. Biol. Chem.* 279(22):22809-22819.
2. Ishida N, *et al.* (2008) Biosynthetic exchange of bromide for chloride and strontium for calcium in the photosystem II oxygen-evolving enzymes. *J. Biol. Chem.* 283(19):13330-13340.
3. Sander J, *et al.* (2010) Functional Characterization and Quantification of the Alternative PsbA Copies in Thermosynechococcus elongatus and Their Role in Photoprotection. *J. Biol. Chem.* 285(39):29851-29856.
4. Schosseler P, Wacker T, & Schweiger A (1994) Pulsed Eldor Detected Nmr. *Chem. Phys. Lett.* 224(3-4):319-324.
5. Reijerse E, Lendzian F, Isaacson R, & Lubitz W (2012) A tunable general purpose Q-band resonator for CW and pulse EPR/ENDOR experiments with large sample access and optical excitation. *J. Magn. Reson.* 214(0):237-243.

6. Messinger J, Badger M, & Wydrzynski T (1995) Detection of one slowly exchanging substrate water molecule in the S_3 state of photosystem II. *Proc. Natl. Acad. Sci. USA* 92:3209-3213.
7. Hillier W, Messinger J, & Wydrzynski T (1998) Kinetic determination of the fast exchanging substrate water molecule in the S_3 state of photosystem II. *Biochemistry* 37(48):16908-16914.
8. Hillier W & Wydrzynski T (2004) Substrate water interactions within the Photosystem II oxygen evolving complex. *Phys. Chem. Chem. Phys.* 6(20):4882-4889.
9. Cox N, *et al.* (2014) Electronic structure of the oxygen-evolving complex in photosystem II prior to O-O bond formation. *Science* 345(6198):804-808.
10. Schweiger A & Jeschke G (2001) *Principles of Pusle Electron Paramagnetic Resonance* (Oxford University Press, Oxford).
11. Cox N, Nalepa A, Lubitz W, & Savitsky A (2017) ELDOR-detected NMR: A general and robust method for electron-nuclear hyperfine spectroscopy? *J. Magn. Reson.* 280:63-78.
12. Cox N, Nalepa A, Pandelia M-E, Lubitz W, & Savitsky A (2015) Chapter Nine - Pulse Double-Resonance EPR Techniques for the Study of Metallobiomolecules. *Methods Enzymol.*, eds Qin PZ & Warncke K (Academic Press), Vol 563, pp 211-249.
13. Cox N, *et al*. (2011) Effect of Ca^{2+}/Sr^{2+} Substitution on the Electronic Structure of the Oxygen-Evolving Complex of Photosystem II: A Combined Multifrequency EPR, ^{55}Mn-ENDOR, and DFT Study of the S_2 State. *J. Am. Chem. Soc.* 133(10):3635-3648.
14. Pérez Navarro M, *et al.* (2013) Ammonia binding to the oxygen-evolving complex of photosystem II identifies the solvent-exchangeable oxygen bridge the manganese tetramer. *Proc. Natl. Acad. Sci. U.S.A* 110(39):15561-15566.
15. Oyala PH, Stich TA, Debus RJ, & Britt RD (2015) Ammonia Binds to the Dangler Manganese of the Photosystem II Oxygen-Evolving Complex. *J. Am. Chem. Soc.* 137(27):8829-8837.
16. Marchiori DA, Oyala PH, Debus RJ, Stich TA, & Britt RD (2018) Structural Effects of Ammonia Binding to the Mn4CaO5 Cluster of Photosystem II. *J. Phys. Chem. B* 122(5):1588-1599.
17. Su JH, *et al.* (2011) The electronic structures of the S_2 states of the oxygen-evolving complexes of photosystem II in plants and cyanobacteria in the presence and absence of methanol. *Biochim. Biophys. Acta* 1807(7):829-840.
18. Pantazis DA, Ames W, Cox N, Lubitz W, & Neese F (2012) Two Interconvertible Structures that Explain the Spectroscopic Properties of the Oxygen-Evolving Complex of Photosystem II in the S_2 State. *Angew. Chem. Int. Ed.* 51(39):9935-9940.
19. Retegan M, *et al.* (2016) A five-coordinate Mn(IV) intermediate in biological water oxidation: spectroscopic signature and a pivot mechanism for water binding. *Chem. Sci.* 7(1):72-84.
20. Krewald V, *et al.* (2015) Metal oxidation states in biological water splitting. *Chem. Sci.* 6(3):1676-1695.
21. Krewald V, *et al.* (2016) Spin State as a Marker for the Structural Evolution of Nature's Water-Splitting Catalyst. *Inorg. Chem.* 55(2):488-501.
22. Haddy A, Lakshmi KV, Brudvig GW, & Frank HA (2004) Q-band EPR of the S_2 state of Photosystem II confirms an S=5/2 origin of the X-band g=4.1 signal. *Biophys. J.* 87(4):2885-2896.
23. Retegan M, Cox N, Pantazis DA, & Neese F (2014) A First-Principles Approach to the Calculation of the on-Site Zero-Field Splitting in Polynuclear Transition Metal Complexes. *Inorg. Chem.* 53(21):11785-11793.
24. Gupta R, *et al.* (2015) High-spin Mn–oxo complexes and their relevance to the oxygen-evolving complex within photosystem II. *Proc. Natl. Acad. Sci. U.S.A* 112(17):5319-5324.
25. Mukherjee S, *et al.* (2012) Synthetic model of the asymmetric $[Mn_3CaO_4]$ cubane core of the oxygen-evolving complex of photosystem II. *Proc. Natl. Acad. Sci. U.S.A* 109(7):2257-2262.
26. Boussac A, Sugiura M, Rutherford AW, & Dorlet P (2009) Complete EPR Spectrum of the S_3-State of the Oxygen-Evolving Photosystem II. *J. Am. Chem. Soc.* 131(14):5050.
27. Boussac A, Sugiura M, Inoue Y, & Rutherford AW (2000) EPR study of the oxygen evolving complex in His-tagged photosystem II from the cyanobacterium *Synechococcus elongatus*. *Biochemistry* 39(45):13788-13799.
28. Boussac A, *et al.* (2018) The low spin-high spin equilibrium in the S_2-state of the water oxidizing enzyme. *Biochim. Biophys. Acta* 1859(5):342-356.
29. Kim CJ & Debus RJ (2017) Evidence from FTIR Difference Spectroscopy That a Substrate H_2O Molecule for O_2 Formation in Photosystem II Is Provided by the Ca Ion of the Catalytic Mn4CaO5 Cluster. *Biochemistry* 56(20):2558-2570.